CANCER

# CKLF instigates a "cold" microenvironment to promote MYCN-mediated tumor aggressiveness

**Xiaodan Qin[1]†, Andrew Lam[1]†, Xu Zhang[1,2]†, Satyaki Sengupta[3], J. Bryan Iorgulescu[4,5], Hongru Ni[1], Sanjukta Das[3,6], Madison Rager[1], Zhenwei Zhou[7], Tao Zuo[8], Grace K. Meara[1], Alexander E. Floru[1], Chinyere Kemet[1], Divya Veerapaneni[1], Daniel Kashy[1], Liang Lin[4], Kenneth Lloyd[9], Lauren Kwok[1], Kaylee S. Smith[1], Raghavendar T. Nagaraju[10,11], Rob Meijers[9], Craig Ceol[12], Ching-Ti Liu[7], Sanda Alexandrescu[13], Catherine J. Wu[4,14], Derin B. Keskin[4,15,16,17,18], Rani E. George[3], Hui Feng[1]***



**Solid tumors, especially those with aberrant MYCN activation, often harbor an immunosuppressive microenvironment to fuel malignant growth and trigger treatment resistance. Despite this knowledge, there are no effective strategies to tackle this problem. We found that chemokine-like factor (*CKLF*) is highly expressed by various solid tumor cells and transcriptionally up-regulated by MYCN. Using the MYCN-driven high-risk neuroblastoma as a model system, we demonstrated that as early as the premalignant stage, tumor cells secrete CKLF to attract CCR4-expressing CD4$^+$ cells, inducing immunosuppression and tumor aggression. Genetic depletion of CD4$^+$ T regulatory cells abolishes the immunorestrictive and protumorigenic effects of CKLF. Our work supports that disrupting CKLF-mediated cross-talk between tumor and CD4$^+$ suppressor cells represents a promising immunotherapeutic approach to battling MYCN-driven tumors.**

## INTRODUCTION

The MYCN oncoprotein drives the initiation, progression, and treatment resistance of a broad spectrum of human cancers (*1*, *2*). Solid tumors with aberrant MYCN activation, particularly high-risk neuroblastoma, are immunologically "cold" and respond poorly to immunotherapy (*1*, *3*–*6*). These cold tumors are characterized by a low mutational burden and few tumor-infiltrating lymphocytes (TILs), particularly cytotoxic CD8$^+$ cells, which is in stark contrast to the immunologically "hot" tumors (*7*–*10*). Strategies that turn cold tumors into immunologically active tumors are heavily sought after to improve the success rate of immunotherapy.

Neuroblastoma is the most common extracranial solid tumor among children, and increased MYCN activity contributes to ~50% of high-risk neuroblastoma (*1*, *11*–*14*). MYCN-driven neuroblastoma metastasizes rapidly with only a 40% 5-year survival rate, representing a clear unmet medical need (*13*, *15*–*17*). MYCN can induce an immunosuppressive tumor microenvironment (TME) by inhibiting the secretion of CXCL10, which, in turn, impedes the recruitment of CD8$^+$ T cells to the TME (*4*). In addition, MYCN represses the expression of CCL2, a key chemokine responsible for the chemoattraction of natural killer (NK) T cells (*18*). MYCN-driven tumors also exhibit reduced activity of the interferon (IFN) pathway, a central component of antitumor immune response (*4*). Despite this knowledge, it remains unknown whether MYCN can induce immunosuppression by up-regulating a chemokine, which can represent an ideal therapeutic target to reverse the protumor milieu to an antitumor TME.

The zebrafish model of MYCN-driven neuroblastoma, in which tumor development intertwines with a gradually maturing immune system, recapitulates the genetic and molecular features of human neuroblastoma (*19*–*23*). To uncover previously inaccessible mechanisms of MYCN-mediated immunosuppression, we integrated analyses of human solid tumors with live tracking and functional studies of the TME in this zebrafish cancer model. We demonstrate that MYCN transcriptionally up-regulates chemokine-like factor (CKLF) to promote the cross-talk between tumor and CCR4-expressing CD4$^+$ cells, thereby cultivating immunosuppression and tumor aggression.

## RESULTS

### CKLF is the most expressed chemokine and predicts patient prognosis across diverse solid tumor types

Most solid tumors harbor a T cell–poor environment, posing a major challenge for immunotherapy (*7*). One class of molecules that modulates the composition of the TME is chemokines, which

[1]Departments of Pharmacology, Physiology & Biophysics and Medicine, Section of Hematology and Medical Oncology, Cancer Research Center, Boston University Chobanian & Avedisian School of Medicine, Boston, MA, USA. [2]Guangdong Key Laboratory for Innovative Development and Utilization of Forest Plant Germplasm, College of Forestry and Landscape Architecture, South China Agricultural University, Guangzhou, China. [3]Department of Pediatric Oncology, Dana-Farber Cancer Institute, Harvard Medical School, Boston, MA, USA. [4]Department of Medical Oncology, Dana-Farber Cancer Institute, Harvard Medical School, Boston, MA, USA. [5]Molecular Diagnostics Laboratory, Department of Hematopathology, Division of Pathology and Laboratory Medicine, The University of Texas MD Anderson Cancer Center, Houston, TX, USA. [6]School of Biotechnology, KIIT University, Bhubanesw, India. [7]Department of Biostatistics, Boston University School of Public Health, Boston, MA, USA. [8]Department of Pathology & Laboratory Medicine, Boston University Chobanian & Avedisian School of Medicine, Boston Medical Center, Boston, MA, USA. [9]Institute for Protein Innovation, Boston, MA, USA. [10]Faculty of Biology, Medicine and Health, Division of Cancer Sciences, University of Manchester, Manchester, UK. [11]Colorectal and Peritoneal Oncology Centre, The Christie NHS Foundation Trust, Manchester, UK. [12]Department of Molecular, Cell and Cancer Biology, Program in Molecular Medicine, University of Massachusetts Medical School, Worcester, MA, USA. [13]Department of Pathology, Boston Children's Hospital, Harvard Medical School, Boston, MA, USA. [14]Department of Medicine, Brigham and Women's Hospital, Harvard Medical School, Boston, MA, USA. [15]Translational Immunogenomics Laboratory, Dana-Farber Cancer Institute, Harvard Medical School, Boston, MA, USA. [16]Section for Bioinformatics, Department of Health Technology, Technical University of Denmark, Lyngby, Denmark. [17]Department of Computer Science, Metropolitan College, Boston University, Boston, MA, USA. [18]Broad Institute of MIT and Harvard, Cambridge, MA, USA.
*Corresponding author. Email: huifeng@bu.edu
†These authors contributed equally to this work.

tumors often secrete to influence the movement and dynamics of immune cells (*24*). Here, we used the Cancer Cell Line Encyclopedia (CCLE) database to screen for tumor cell–expressing chemokines that may contribute to an immunorestrictive TME (*25*). Analysis of 1108 cell lines across 84 types of solid tumors uncovered CKLF as the most highly expressed chemokine (Fig. 1, A and B, and fig. S1) (*26*, *27*). Next, we leveraged four online platforms (the R2: Genomics Analysis and Visualization Platform, Survival Genie, cBioPortal, and Kaplan-Meier plotter) to assess the association of *CKLF* and two other top-expressed chemokines with patient survival (*28*–*32*). The median expression of *CKLF*, *CXCL16*, and *CXCL1* was used to categorize patients into low- and high-expression groups. Kaplan-Meier analysis revealed that unlike *CXCL16* or *CXCL1*, elevated *CKLF* expression was primarily linked with poor patient survival in immunologically cold tumors for which survival data were available (Fig. 1C and tables S1 to S3). Among these tumors, the association of *CKLF* expression with poor patient survival was most apparent for neuroblastoma and glioma (Fig. 1, C and D, fig. S2A, and table S1), in which MYCN drives tumor aggressiveness (*1*, *2*). Higher *CKLF* expression in neuroblastoma was linked to *MYCN* amplification, advanced disease stage, older patient age, and high-risk disease (fig. S2, B to G). We also observed the association of high *CKLF* expression with poor survival of *MYCN* nonamplified patients (Fig. 1E and fig. S2H). Patients with *MYCN* amplification tend to have the poorest survival (*33*); *CKLF* expression was able to somewhat further segregate the prognosis of these patients (fig. S2I). On the other hand, *CXCL16* and *CXCL1*—the second and third most highly expressed—showed the opposite or no association with neuroblastoma patient survival, respectively (Fig. 1C and tables S2 and S3). Collectively, these analyses demonstrate that *CKLF* is the most expressed chemokine across various solid tumor types and predicts poor patient prognosis in multiple cold tumors.

### CKLF is transcriptionally up-regulated by MYCN and secreted by tumor cells to attract CCR4-expressing $CD4^+$ cells and forkhead box P3 $(FOXP3)^+$ regulatory T cells in particular

Given the critical role of both MYCN and MYC in driving tumor aggressiveness (*34*), we assessed their relationship with CKLF using RNA sequencing data from 498 human primary neuroblastoma samples (GSE49711) (*35*). We applied the 87-gene *MYCN* signature score and the 18-gene *MYC* signature score that were previously published for this analysis (*36*, *37*). Consistent with the importance of both oncogenes in neuroblastoma genesis (*38*, *39*), the *CKLF* score was positively correlated with both *MYCN* and *MYC* signature score (Fig. 2A) (*36*, *37*). Since the contribution of MYCN to immunosuppression is well established in neuroblastoma (*4*–*6*, *18*, *40*), we focused our study on the molecular connection between MYCN and CKLF. To understand whether MYCN transcriptionally up-regulates CKLF, we examined chromatin immunoprecipitation sequencing (ChIP-seq) data from human SHEP neuroblastoma cells in which exogenous MYCN expression is induced (on) or inhibited (off) by tetracycline (tet) (*41*, *42*). We found that MYCN binds to the promoter regions of *CKLF* and increases histone acetylation signals, indicating transcriptional activation of *CKLF* by MYCN (Fig. 2B). To validate this prediction, we measured *CKLF* transcript levels in human SHEP–MYCN–estrogen receptor (ER) neuroblastoma cells, in which 4-hydroxytamoxifen (4OHT) conditionally activates MYCN (*43*). MYCN activation upon 4OHT treatment significantly up-regulated the expression of *CKLF* at the same time points as a known MYCN target gene *NPM1* (Fig. 2C and fig. S3).

Next, we measured CKLF protein levels in the culture medium of the SHEP-MYCN-ER cells and detected a significant increase upon MYCN activation (Fig. 2D), indicating that MYCN activation in these tumor cells leads to increased CKLF secretion. Since neuroblastoma formation requires the recruitment of $CD4^+$ cells to the TME, we applied a coculturing system to determine how CKLF affects T cell recruitment to MYCN-activated tumors (Fig. 2E). The CKLF-containing medium from 4OHT-treated SHEP-MYCN-ER cells recruited more $CD4^+$ and regulatory T cells ($T_{reg}$ cells) but not $CD8^+$ cells (Fig. 2F and fig. S4, A and B). The C-terminal peptides of CKLF1 (i.e., a secreted isoform of CKLF), C27 and C19, bind to the chemokine receptor CCR4 (*44*), which is expressed on the surface of $CD4^+$ cells, including $T_{reg}$ cells (*45*). To assess whether the CKLF-CCR4 interaction contributes to the recruitment of $CD4^+$ cells, we supplemented the medium with C27 and C19 in the lower chamber of transwell plates and quantified lymphocytes that migrated to the lower chamber (Fig. 2E). Notably, both C27 and C19 peptides significantly enhanced the migration of $CD4^+$ and $T_{reg}$ cells, but not $CD8^+$ T cells, with the longer peptide C27 showing better chemotaxis (Fig. 2G and fig. S4, C and D). Moreover, the chemotaxis effect of C27 on $CD4^+$ and $T_{reg}$ cells was dampened by pretreating lymphocytes with the Food and Drug Administration–approved CCR4 antagonist mogamulizumab (fig. S5).

To assess the relationship between MYCN, CKLF, and $T_{reg}$ cells in primary patient samples, we performed immunohistochemical staining to detect protein expression of MYCN, CKLF, and the $T_{reg}$ marker FOXP3. As expected, MYCN protein levels were significantly higher in tumors with *MYCN* amplification, with CKLF following the same trend (fig. S6 and table S4). In addition, CKLF expression was significantly elevated in all primary tumor samples with high MYCN levels but barely detectable in most tumor samples with low MYCN expression (Fig. 2H, fig. S7, and table S4). Occasionally, CKLF expression was detected in patient neuroblastoma cells without concurrent MYCN expression (table S4), suggesting the existence of additional regulators of CKLF other than MYCN. Consistent with our findings in the in vitro coculturing assay, $FOXP3^+$ T cells were significantly enriched in tumors with high MYCN and CKLF expression compared to those with low expression, indicating the recruitment of $T_{reg}$ cells by CKLF (Fig. 2H, fig. S7, and table S4). Together, our findings demonstrate that human neuroblastoma cells up-regulate CKLF through MYCN and secrete this chemokine to attract $CD4^+$ and $FOXP3^+$ $T_{reg}$ cells through CCR4.

### TME tracking in zebrafish demonstrates similarities to human disease and reveals tumor stage–specific and developmental oscillations

The zebrafish model of MYCN-driven neuroblastoma, referred to as *MYCN;EGFP*, in which human *MYCN* and *EGFP* genes are coexpressed under the zebrafish dopamine β hydroxylase (*dβh*) promoter, develops tumors in the interrenal gland (the analogous location of the human adrenal medulla) (*19*). To assess the molecular relationship between MYCN and CKLF in the zebrafish neuroblastoma model, we studied tumors from *MYCN;EGFP* siblings that developed either localized or metastatic disease (Fig. 3A). An approximately fourfold increase in MYCN protein levels was detected in primary tumors from zebrafish with metastatic tumors (PT-FM) compared to those from sibling fish with localized disease (PT-FL) (Fig. 3B). This

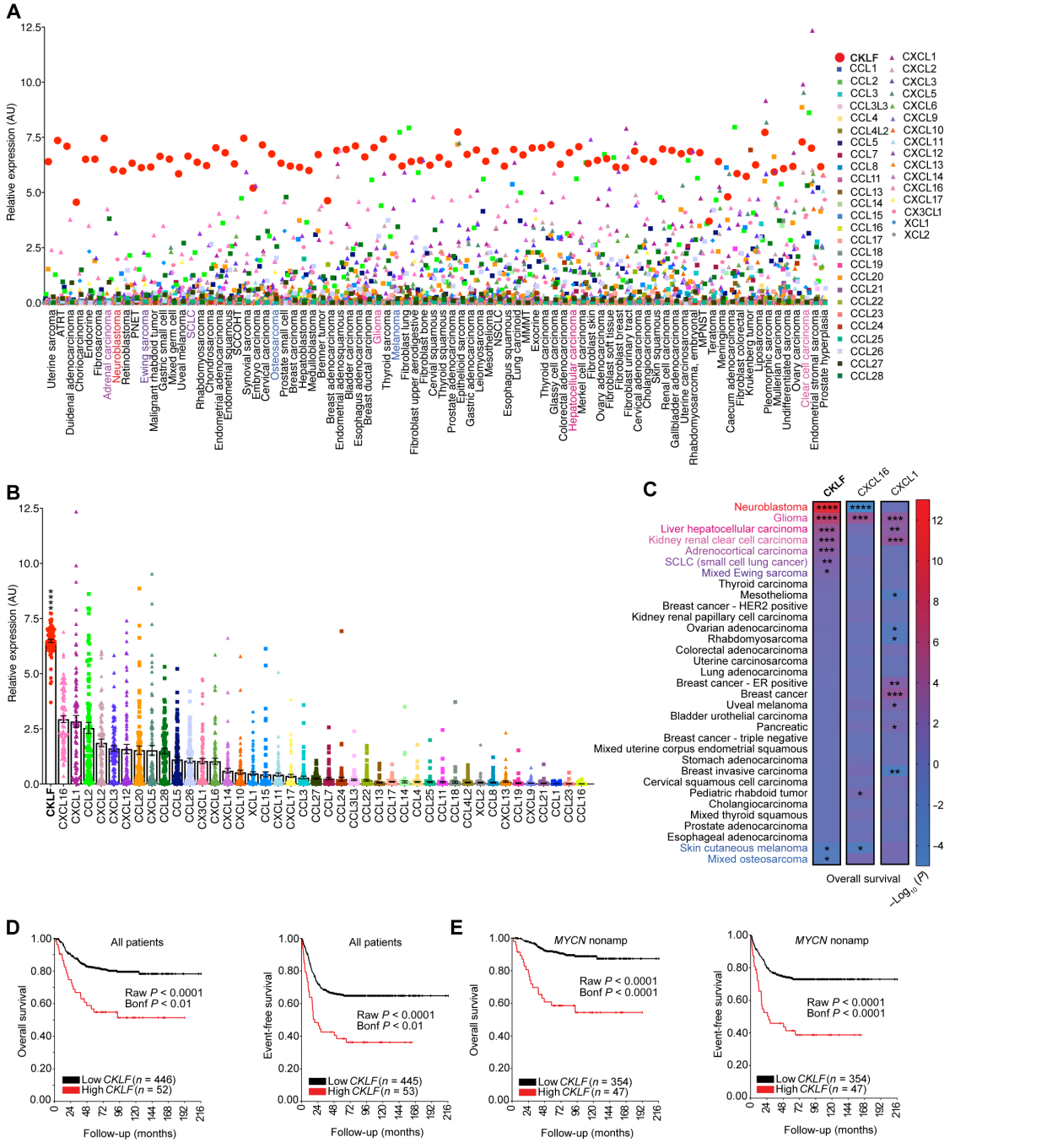


**Fig. 1. *CKLF* is the most expressed chemokine and predicts patient prognosis across diverse solid tumor types.** (**A** and **B**) Normalized relative expression (A) and quantification (B) of all chemokines annotated in the CCLE database, containing 1108 human cancer cell lines across 84 types of solid tumors (*25*). The ratios of the average expression of *CKLF* to other chemokines were used to rank order each cancer type. Dots denote the mean expression value of each chemokine in multiple cell lines from the same cancer type. AU, arbitrary units; SCLC, small cell lung cancer; ATRT, atypical yeratoid/rhabdoid tumor; PNET, primitive neuroectodemal tumor; SCCOHT, small cell carcinoma of the ovary, hypercalcemic type; NSCLC, non-small cell lung cancer; MMMT, malignant mix Müllerian tumor. (**C**) Kaplan-Meier analysis of the association of the top three expressed chemokines, *CKLF*, *CXCL16*, and *CXCL1*, with patient overall survival across multiple solid tumors. Patients were dichotomized into high-expressing versus low-expressing groups based on the median expression value of each chemokine. The overall survival was compared between the two groups of patients using a log-rank test, with the *P* values depicted as $-\log_{10}(P$ values). Red or purple color indicates the association of the high chemokine expression with worse patient survival, while blue color denotes better survival. Data were obtained from the four online platforms: R2: Genomics Analysis and Visualization Platform, Survival Genie, cBioPortal, and Kaplan-Meier plotter (tables S1 to S3) (*28*–*32*). HER2, Human Epidermal Growth Factor Receptor 2. (**D** and **E**) Kaplan-Meier curves showing the association of *CKLF* expression with overall (left) and event-free (right) (i.e., no occurrence of cancer progression, relapse, or patient death) survival of all (D) or *MYCN* nonamplified (Nonamp) (E) patients with neuroblastoma, using the R2 Kaplan-Meier scan method to categorize patients (GSE49710) (*81*). Data in (B) are presented as means ± SEM and compared for statistical significance by an unpaired two-tailed *t* test. **P* < 0.05, ***P* < 0.01, ****P* < 0.001, and *****P* < 0.0001.

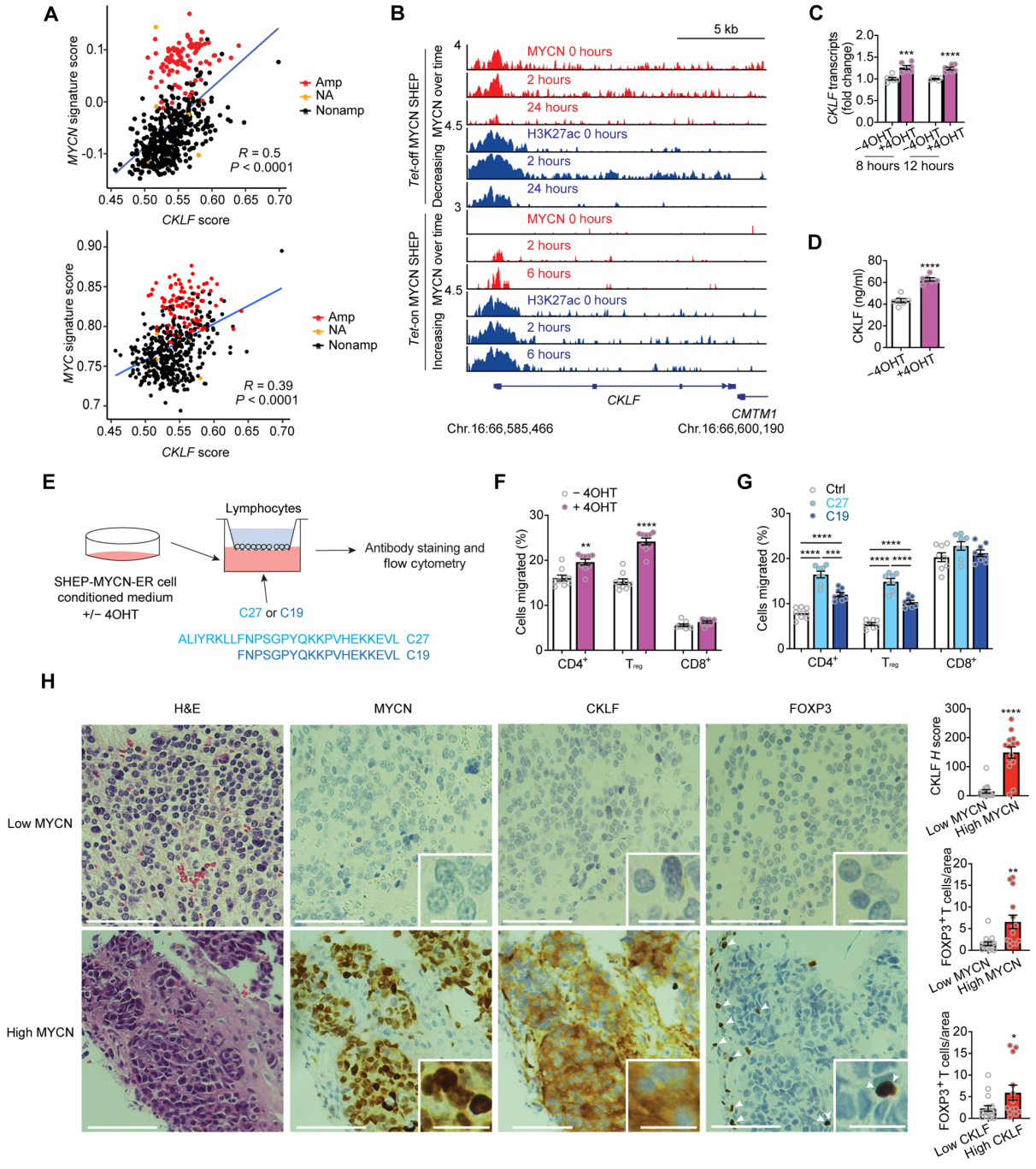


**Fig. 2. MYCN transcriptionally up-regulates CKLF in human neuroblastoma cells to attract CD4$^+$ cells, especially FOXP3$^+$ T$_{reg}$ cells.** (**A**) Scatter plots depicting the Pearson correlation between *CKLF* and *MYCN* (top) or *MYC* (bottom) signature scores in neuroblastoma patient samples (red: Amp, *MYCN*-amplified; yellow: NA, information not available; and black: Nonamp, *MYCN* nonamplified). (**B**) Reanalysis of ChIP-seq database for the MYCN and active chromatin acetylation (H3K27ac) signals at the *CKLF* promoter in human *Tet*-on or *Tet*-off MYCN SHEP neuroblastoma cells (GSE80151) (*42*). (**C**) Quantitative real-time polymerase chain reaction (qRT-PCR) to detect transcript levels of *CKLF* in human SHEP-MYCN-ER cells with or without 4OHT treatment for 8 or 12 hours ($n = 6$). (**D**) Enzyme-linked immunosorbent assay (ELISA) detection of CKLF in the medium secreted by human SHEP-MYCN-ER cells with or without 4OHT treatment for 48 hours ($n = 6$). (**E**) Schematic of the transwell migration assay. The sequences of two CKLF1 C-terminal peptides (C27 and C19, blue) are shown. (**F** and **G**) Percentages of human CD4$^+$, T$_{reg}$, and CD8$^+$ T cells migrated to the lower chamber of the plate, containing medium of human SHEP-MYCN-ER cells treated with or without 4OHT for 48 hours (F) ($n = 9$) or supplemented with CKLF1 synthetic C27 or C19 peptides (G) ($n = 8$). (**H**) Representative histological and immunohistochemical staining (brown) and quantification of MYCN (nuclear), CKLF (cytoplasm), and FOXP3 (nuclear) in primary neuroblastoma patient samples (excluding immune niches; $n = 16$ and 14 for MYCN-low and -high samples and $n = 17$ and 13 for CKLF-low and -high samples). H&E, hematoxylin and eosin. Inserts: Zoom-in views. Arrowheads: FOXP3$^+$ T cells. Scale bars, 200 and 50 μm (inserts). *n* indicates experimental [(C) to (G)] or biological replicates (H). Data [(C) to (H)] are presented as means ± SEM and compared with unpaired two-tailed *t* tests. Representative of two [(C), (D), (F), and (G)] experiments. *$P < 0.05$, **$P < 0.01$, ***$P < 0.001$, and ****$P < 0.0001$.

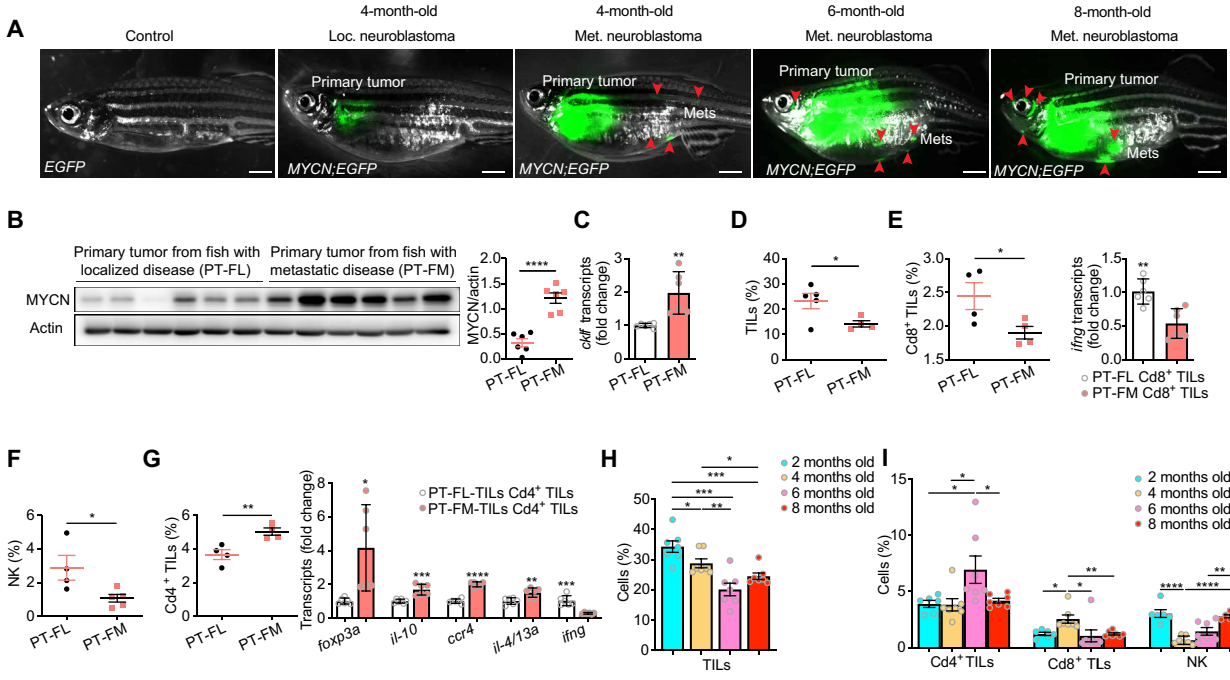


**Fig. 3. The zebrafish model of MYCN-driven neuroblastoma resembles human disease and harbors a cold TME enriched with Cd4$^+$ Foxp3$^+$ T$_{reg}$ cells as tumors progress.** (**A**) Overlay of brightfield and enhanced green fluorescent protein (EGFP) images of representative control *Tg(dβh:EGFP)* and *Tg(dβh:MYCN;dβh:EGFP)* zebrafish, referred to as *EGFP* and *MYCN;EGFP*, respectively, at 4 months old. Representative images of 4-, 6-, and 8-month-old *MYCN;EGFP* fish with metastatic tumor are shown. EGFP signals enable visualization and quantification of tumors, and red arrowheads point to metastatic tumors. Scale bars, 1 mm. (**B**) Western blotting analysis (left) and quantification (right) of MYCN protein levels in the primary tumor isolated from individual *MYCN;EGFP* sibling fish that developed either PT-FL or PT-FM at 4 months of age ($n$ = 6). Actin serves as the loading and normalization control. (**C**) Relative *cklf* expression, detected by qRT-PCR, in PT-FL versus PT-FM ($n$ = 6). (**D** to **G**) Flow cytometric analysis of TILs (D), Cd8$^+$ (E, left), NK (F), and Cd4$^+$ (G, left) TILs in PT-FL or PT-FM that express low or high *MYCN* and *cklf*, respectively ($n$ = 4 or 5). qRT-PCR to detect relative expression of *ifng* in Cd8$^+$ TILs (E, right) and *foxp3a*, *il-10*, *ifng*, *il-4/13a*, and *ccr4* expression in Cd4$^+$ TILs (G, right) from the above two groups ($n$ = 6). (**H** and **I**) Flow cytometric analysis of total TILs (H), Cd4$^+$, Cd8$^+$, and NK cell percentages (I) in the TME of primary tumors from *MYCN;EGFP* fish at the indicated age ($n$ = 6 or 7). $n$ indicates biological [(B) and (D) to (I)] or experimental (C) replicates. [(B) to (G)] Representative of two experiments as means ± SEM and compared with unpaired two-tailed $t$ tests. *$P$ < 0.05, **$P$ < 0.01, and ****$P$ < 0.0001.

result faithfully reproduces what is observed in human disease, in which high *MYCN* expression is associated with advanced disease and poor prognosis (*46*). Furthermore, ChIP–polymerase chain reaction (PCR) assays using PT-FM revealed that MYCN binds to the promoter regions of *cklf* and *npm1* significantly more than *cxcl12a*, a non–MYCN target gene (fig. S8A) (*47*). Correspondingly, quantitative real-time PCR (qRT-PCR) showed an increase in *cklf* transcript levels in PT-FM with elevated MYCN expression compared to the PT-FL (Fig. 3C).

Human MYCN-driven neuroblastomas are immunologically cold and characterized by few TILs (*4*). To understand how the TME is modulated during tumor development and progression, we characterized the PT-FL and PT-FM from sibling zebrafish to minimize age-induced immune changes. We detected a significantly lower percentage of TILs, as well as Cd8$^+$ T and NK cells, in PT-FM compared to PT-FL (Fig. 3, D to F, and figs. S8B and S9, A to C). Consistent with data from human tumor samples (*4*), Cd8$^+$ TILs from PT-FM also exhibited decreased *ifng* expression. Although the frequency of Cd4$^+$ T cells is slightly higher in PT-FM, they are immunosuppressive, as demonstrated by increased expression of T$_{reg}$ marker genes, *foxp3a* and *il-10* (*48*), as well as decreased expression of *ifng* (Fig. 3G and figs. S8C and S9B). Next, we analyzed *MYCN;EGFP* fish of different ages, with older fish developing more metastases (Fig. 3A and fig. S10). The percentages of TILs declined as fish aged and tumors progressed, with a significant decrease in 6- and 8-month-old fish compared to younger fish (Fig. 3H and fig. S9D). Among the TILs, Cd4$^+$ cells comprised a larger proportion than Cd8$^+$ and NK cells, peaking at 6 months and declining at 8 months (Fig. 3I and fig. S9, E and F). As expected, frequencies of both Cd8$^+$ and NK cells in the TME were low: Cd8$^+$ cells peaked at 4 months, while NK cells dropped initially and then rose moderately with age (Fig. 3I). Together, our findings in zebrafish reveal disease stage–specific and developmental oscillations of TME and demonstrate the similarities of our zebrafish model to patient neuroblastoma (*4*), with aggressive tumors expressing high MYCN/CKLF and harboring a cold TME enriched with CD4$^+$ T$_{reg}$ cells.

## CKLF collaborates with MYCN to recruit CD4$^+$ cells, drive immunosuppression, and promote tumor aggressiveness

To characterize the functional importance of CKLF in MYCN-mediated immunosuppression, we overexpressed *cklf* (*cklf_OE*) in zebrafish neural crest cells to mimic high CKLF expression in aggressive patient tumors (*49*). Specifically, we injected *dβh:cklf* construct into the one–cell stage embryos from the *EGFP* or *MYCN;EGFP* fish crossed with the *Tg(cd4-1:mCherry)* fish (Fig. 4A and fig. S11A). The differential fluorescence labeling of immune cells and neuroblasts with mCherry and EGFP, along with the optical transparency of zebrafish, enabled us to monitor the dynamic

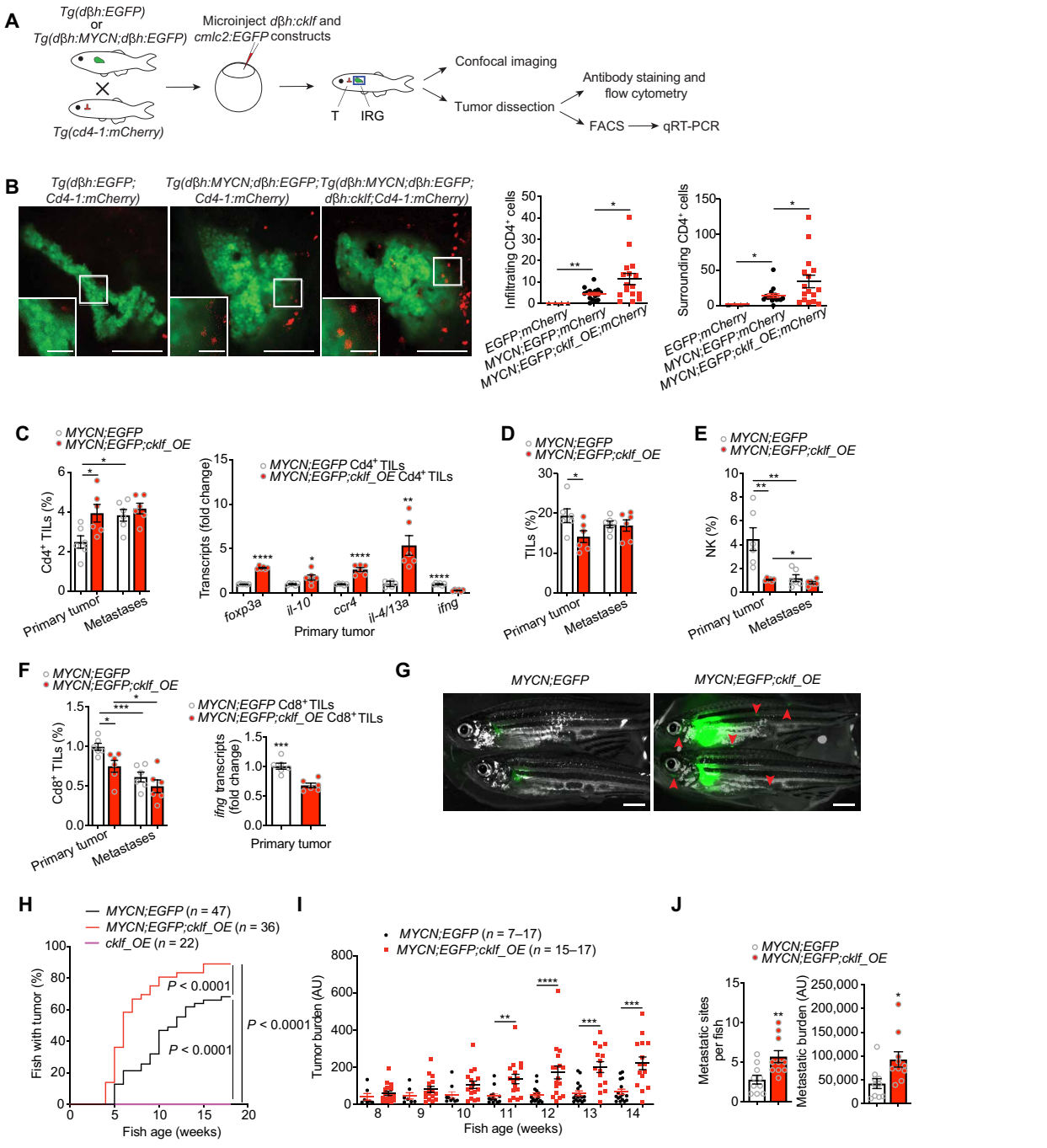


**Fig. 4. CKLF collaborates with MYCN to recruit CD4$^+$ cells, induce an immunosuppressive TME, and promote neuroblastoma aggressiveness.** (**A**) Schematic of experimental flow. T, thymus; IRG, interrenal glands. (**B**) Overlay of EGFP and red fluorescent protein images at the interrenal gland of *Tg(dβh:EGFP;Cd4-1:mCherry)*, *Tg(dβh:MYCN;dβh:EGFP;Cd4-1:mCherry)*, and *Tg(dβh:MYCN;dβh:EGFP;dβh:cklf;Cd4-1:mCherry)* fish, referred to as *EGFP;mCherry*, *MYCN;EGFP;mCherry*, and *MYCN;EGFP;cklf_OE;mCherry*, respectively. Scale bars, 100 and 25 μm (inserts). Quantification of Cd4$^+$ cells surrounding or infiltrating EGFP$^+$ neural crest or premalignant mass ($n = 4$ or 16). (**C**) Quantification and characterization of Cd4$^+$ TILs from primary or metastatic tumors of 6-month-old *MYCN;EGFP* and *MYCN;EGFP;cklf_OE* fish ($n = 6$). qRT-PCR to detect *foxp3a*, *il-10*, *ifng*, *il-4/13a*, and *ccr4* expression in Cd4$^+$ TILs ($n = 6$). (**D** to **F**) Flow cytometric analysis of TILs (D), NK cells (E), and Cd8$^+$ TILs (F) of the primary or metastatic tumors from 6-month-old *MYCN;EGFP* versus *MYCN;EGFP;cklf_OE* fish ($n = 6$). qRT-PCR to detect relative *ifng* expression of Cd8$^+$ TILs purified by fluorescent-activated cell sorting (FACS) (F) ($n = 6$, right) from *MYCN;EGFP* and *MYCN;EGFP;cklf_OE* primary tumors. (**G**) Overlay of brightfield and EGFP images of 9-week-old *MYCN;EGFP* (left) and *MYCN;EGFP;cklf_OE* (right) fish. Scale bars, 2 mm. (**H**) Kaplan-Meier analysis of rates of neuroblastoma development in *MYCN;EGFP* (black line; $n = 47$), *MYCN;EGFP;cklf_OE* (red line; $n = 36$), and *cklf_OE* fish (purple line; $n = 22$). (**I**) Quantification of tumor burden over time based on EGFP intensity of *MYCN;EGFP* ($n = 7$ to 17) and *MYCN;EGFP;cklf_OE* fish ($n = 15$ to 17). (**J**) Metastases quantification in *MYCN;EGFP* and *MYCN;EGFP;cklf_OE* fish ($n = 10$). *n* indicates biological replicates [(B) to (J)]. Representative of two [(C) to (F) and (I)] or pooled [(B) and (H)] experiments. (H) was analyzed using log-rank Mantel-Cox test. [(B) to (F) and (I)] Data are presented as means ± SEM and compared with unpaired two-tailed *t* tests. *$P < 0.05$, **$P < 0.01$, ***$P < 0.001$, and ****$P < 0.0001$.

interactions between immune and malignant cells at different ages of fish (*50*). We found that $Cd4^+$ cells did not migrate toward the neural crest regions in fish at 1 week of life (figs. S11B and S12, A and B). However, both macrophages and neutrophils had already infiltrated the *MYCN*-overexpressing premalignant mass (fig. S12, A and B), when imaging the progeny from *Tg(mepg1:mCherry)* or *Tg(lysc:mCherry)* fish crossed to *EGFP* or *MYCN;EGFP* fish (*51*, *52*). By 2 weeks, $Cd4^+$ cells began to infiltrate the premalignant mass in both *MYCN;EGFP;mCherry* and *MYCN;EGFP;cklf_OE;mCherry* fish (fig. S11C). Ectopic expression of *cklf* did not increase the frequency of $Cd4^+$ cells in the premalignant mass of 1- or 2-week-old fish (fig. S11, B and C). By 3 weeks, significantly more $Cd4^+$ cells encompassed and penetrated the premalignant mass of *MYCN;EGFP;mCherry* fish compared to the age-matched *EGFP;mCherry* fish (Fig. 4B). We detected twice as many $Cd4^+$ cells in the TME of *MYCN;EGFP;cklf_OE;mCherry* fish than was seen in *MYCN;EGFP;mCherry* fish at 3 weeks of age (Fig. 4B). Hence, tracking the TME by live imaging enabled us to monitor the initial infiltration of immune cells and uncover the ability of Cklf in recruiting $Cd4^+$ cells before tumor formation.

Next, we asked whether CKLF could increase the frequency of $Cd4^+$ cells in established tumors. Despite similar MYCN levels, overexpression of *cklf* significantly enriched $Cd4^+$ cells in primary tumors from *MYCN;EGFP;cklf_OE* fish, compared to those from their sibling *MYCN;EGFP* fish (Fig. 4C and figs. S11D and S13A). Molecular characterization revealed high expression of $T_{reg}$ marker gene *foxp3a* and *il-10* in $Cd4^+$ TILs purified from *MYCN;EGFP;cklf_OE* primary tumors, indicating the enrichment of $T_{reg}$ cells in the TME. We also detected a higher level of *ccr4* and *il-4*, along with decreased expression of *ifng* (Fig. 4C). Consistent with their enrichment of $T_{reg}$ cells, the percentage of TILs in *MYCN;EGFP;cklf_OE* primary tumors was lower compared to those in the *MYCN;EGFP* fish (Fig. 4D and fig. S13B). In particular, the frequencies of cytotoxic NK and $Cd8^+$ cells in primary tumors overexpressing *cklf* were significantly lower than those in *MYCN;EGFP* fish (Fig. 4, E and F, and figs. S11E and S13, A and C). In addition, $Cd8^+$ TILs from *cklf*-overexpressing primary tumors had lower levels of *ifng* (Fig. 4F), further indicating a role of CKLF in enhancing immunosuppression. Next, we characterized lymphocyte infiltration in primary versus metastatic tumors from individual *MYCN;EGFP* and *MYCN;EGFP;cklf_OE* fish. Metastatic tumors had an increased percentage of $Cd4^+$ TILs yet decreased $Cd8^+$ TILs and NK cells compared to primary tumors in *MYCN;EGFP* fish (Fig. 4, C to F, and fig. S13, A and C). Unexpectedly, there were no differences in $Cd4^+$ TILs but a slight decrease in $Cd8^+$ TILs and NK cells in metastatic tumors compared to primary tumors from *MYCN;EGFP;cklf_OE* fish (Fig. 4, C to F, and fig. S13, A and C). The lymphocyte infiltration property of primary tumors from the *MYCN;EGFP;cklf_OE* fish closely resembled that of metastases in the *MYCN;EGFP* fish (Fig. 4, C to F), indicating that increased *cklf* expression may induce a TME favoring metastatic spread.

Last, we asked whether CKLF can potentiate MYCN-mediated tumor aggressiveness. Although ectopic expression of *cklf* alone was insufficient to induce tumors, *MYCN;EGFP;cklf_OE* fish exhibited faster and more frequent tumor development than *MYCN;EGFP* fish, despite similar levels of MYCN expression in their neuroblasts (Fig. 4, G to I, and fig. S11D). By 4 weeks of life, ~15% of *MYCN;EGFP;cklf_OE* fish developed tumors, whereas none of their *MYCN;EGFP* siblings did (Fig. 4H). By 17 weeks, tumors arose in 89% of *MYCN;EGFP;cklf_OE* fish, in contrast to only 68% of *MYCN;EGFP* fish (Fig. 4H). Quantification of the EGFP intensity demonstrated a significantly heavier tumor burden in *MYCN;EGFP;cklf_OE* fish compared to *MYCN;EGFP* fish (Fig. 4, G and I), indicating the ability of CKLF to advance MYCN-driven tumor progression. As expected, overexpression of *cklf* in neural crest cells significantly increases metastatic spread and burden (Fig. 4J), demonstrating the ability of CKLF in promoting tumor aggressiveness at both primary and metastatic sites. Together, live-tracking and functional studies of zebrafish demonstrate that CKLF collaborates with MYCN to recruit and enrich $CD4^+$ cells in the TME, an event that occurs as early as the premalignant stage, leading to immunosuppression and tumor aggressiveness.

### Depleting $T_{reg}$ cells abolishes the protumor and immunosuppressive effects of CKLF

Considering our demonstration that CKLF markedly accelerates tumor initiation and progression while capable of attracting $CD4^+$ $FOXP3^+$ $T_{reg}$ cells to the TME, we next asked whether $T_{reg}$ cells contributed to CKLF-induced tumor aggressiveness and immunosuppression. The transcription factor FOXP3 is crucial for the development and immunosuppression of $T_{reg}$ cells (*53*), and its expression in neuroblastoma is undetectable (Fig. 2H and figs. S7 and S14A). In zebrafish, allelic loss of *foxp3a* reduces $T_{reg}$-like cells without causing obvious developmental defects (fig. S14B) (*54*). Therefore, we overexpressed *cklf* through transgenesis in neural crest of *MYCN;EGFP* and *MYCN;EGFP;foxp3a*$^{+/-}$ fish. Consistent with our earlier findings, *cklf* collaborated with MYCN to promote tumor initiation and progression in sibling fish without *foxp3a* loss (Fig. 5, A to C). Notably, disrupting the development of $T_{reg}$ cells through *foxp3a* loss was sufficient to abolish the ability of Cklf to promote neuroblastoma aggressiveness, as *MYCN;EGFP;foxp3a*$^{+/-}$*;cklf_OE* fish could no longer expedite tumor initiation or progression (Fig. 5, A to C). While 83% of *MYCN;EGFP;cklf_OE* fish developed tumors at 15 weeks of life, only 38% of *MYCN;EGFP;cklf_OE;foxp3a*$^{+/-}$ fish had tumors (Fig. 5B). Depleting $T_{reg}$ cells in *MYCN;EGFP* fish also delayed tumor onset and progression, despite similar MYCN expression in tumor cells (Fig. 5, A and B, and fig. S14C). By 15 weeks, 60% of *MYCN;EGFP* fish had developed tumors, compared to 30% of *MYCN;EGFP;foxp3a*$^{+/-}$ fish (Fig. 5B). In addition, fluorescence microscopy imaging documented that tumors in *MYCN;EGFP* fish grew faster than those in their *MYCN;EGFP;foxp3a*$^{+/-}$ siblings (Fig. 5C).

Next, we asked whether $T_{reg}$ cells contributed to CKLF-induced immunosuppression, as reflected by the reduced $Cd8^+$ and NK cells in the TME. To address this question, we first quantified the frequency of total TILs in primary tumors from all four fish groups and found that depleting $T_{reg}$ cells through *foxp3a* loss was sufficient to completely restore TILs in both fish groups regardless of *cklf* overexpression (Fig. 5D and fig. S15A). In addition, significantly higher frequencies of $Cd4^+$ TILs were detected in the TME of *MYCN;EGFP;foxp3a*$^{+/-}$, *MYCN;EGFP;cklf_OE*, and *MYCN;EGFP;cklf_OE;foxp3a*$^{+/-}$ fish than *MYCN;EGFP* fish (Fig. 5E and fig. S15B). $Cd4^+$ TILs from *MYCN;EGFP;foxp3a*$^{+/-}$ primary tumors were more immunoreactive than those from *MYCN;EGFP* tumors, as demonstrated by reduced *il-10* and increased *ifng* expression (fig. S16B). Moreover, there are more $Cd8^+$ TILs and NK cells in the TME of *MYCN;EGFP;foxp3a*$^{+/-}$ and *MYCN;EGFP;cklf_OE;foxp3a*$^{+/-}$ fish than *MYCN;EGFP* and *MYCN;EGFP;cklf_OE* fish (Fig. 5E and figs. S15, C and D, and S16A). $Cd8^+$ TILs from *MYCN;EGFP;foxp3a*$^{+/-}$ tumors showed up-regulated *ifng* expression, indicating improved cytotoxicity (fig. S16C). In

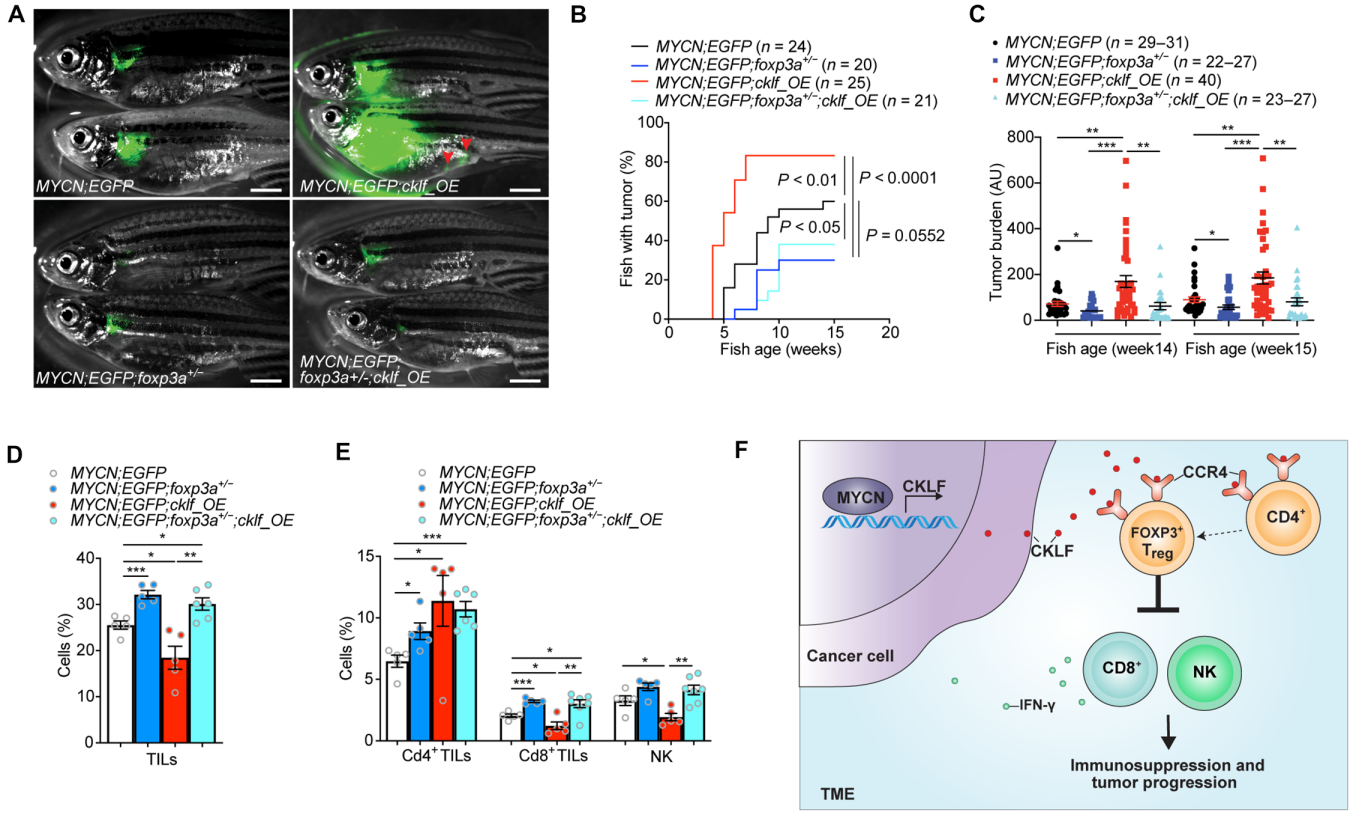


**Fig. 5. Depleting $T_{reg}$ cells abrogates the effects of *cklf* on enhancing neuroblastoma aggressiveness and immunosuppression.** (**A**) Representative overlay of bright-field and EGFP images of *MYCN;EGFP* (top left), *MYCN;EGFP;cklf_OE* (top right), *MYCN;EGFP;foxp3a*$^{+/-}$ (bottom left), and *MYCN;EGFP;foxp3a*$^{+/-}$*;cklf_OE* (bottom right) fish at 7 weeks old. Scale bars, 2 mm. (**B**) Rates of tumor onset for *MYCN;EGFP* (black line; $n = 24$), *MYCN;EGFP;cklf_OE* sibling fish (red line; $n = 25$), *MYCN;EGFP;foxp3a*$^{+/-}$ (dark blue line; $n = 20$), and *MYCN;EGFP;foxp3a*$^{+/-}$*;cklf_OE* (light blue line; $n = 21$). (**C**) Quantification of tumor burden based on EGFP intensity of neuroblastoma from the four fish groups at 14 and 15 weeks old ($n = 22$ to 40). (**D** and **E**) Flow cytometric analysis and quantification of total TILs (D), Cd4$^+$ TILs, Cd8$^+$ TILs, and NK cells (E) from the TME of neuroblastoma dissected from the above fish groups at 6 months of age ($n = 5$ to 7). (**F**) Schematic image depicting the proposed working model to describe our findings. *n* indicates the number of biological replicates [(B) to (E)]. Data are representative of two experiments [(B), (D), and (E)] or pooled from two experiments (C). Survival curves in (B) were compared in a pairwise manner using the log-rank Mantel-Cox test. Data in [(C) to (E)] are presented as means ± SEM and compared to an unpaired two-tailed *t* test. *$P < 0.05$, **$P < 0.01$, and ***$P < 0.001$.

contrast to the TME, the percentages of Cd4$^+$ TILs were similar in the kidneys among these two groups of fish, indicating that the enhancement of immune responses is tumor-specific (fig. S16D). Together, our findings establish the critical role of CD4$^+$ FOXP3$^+$ $T_{reg}$ cells in mediating CKLF-elicited tumor aggressiveness and immunosuppression.

## DISCUSSION

Our research used high-risk neuroblastoma as a model to unravel the mechanisms by which solid tumors cultivate an immunorestrictive TME to favor cancer growth. Our data indicate that MYCN transcriptionally up-regulates *CKLF*, which is secreted into tumor parenchyma to repress the infiltration and cytotoxicity of CD8$^+$ and NK cells through CD4$^+$ FOXP3$^+$ $T_{reg}$ cells, thus promoting immunosuppression and disease aggression (Fig. 5F). The induction of such a tumor-favoring milieu by the MYCN-CKLF-$T_{reg}$ axis may be achieved through (i) the increased chemotaxis of CCR4-expressing $T_{reg}$ cells by tumor-secreted CKLF, (ii) the recruitment of CCR4-expressing naïve CD4$^+$ cells by CKLF to the TME where they differentiate into $T_{reg}$ cells, (iii) the enhanced immunosuppressive activity of $T_{reg}$ cells through the CKLF-CCR4 interaction, and (iv) the cross-talk between $T_{reg}$ cells and myeloid-derived suppressor cells/dendritic cells within the TME (*55*–*58*). In contrast to earlier findings that MYCN inhibits chemokine expression to restrict lymphocyte recruitment (*4*, *18*, *40*), our work provides the first example that MYCN can activate the chemokine CKLF to attract CD4$^+$ immune cells to the TME and induce immunosuppression.

It is well established that MYCN drives tumor initiation and progression through multiple mechanisms, including reprogramming of cellular metabolism (*59*), suppression of estrogen receptor alpha to block neural differentiation (*60*), and inducing an immunosuppressive TME (*4*, *5*, *18*). Hence, it is expected that *cklf* overexpression alone is insufficient to induce tumorigenesis, a cumulative outcome of abnormal intracellular and intercellular events (*61*). Our pan-cancer cell line analyses demonstrated the broad expression of CKLF across 84 solid tumor types, including those not driven by MYCN. In addition, high *CKLF* expression predicted poor patient prognosis in both MYCN-driven and non-MYCN–driven cancers, such as kidney renal clear cell carcinoma. These data suggest that genes other than MYCN could up-regulate CKLF to induce immunosuppression in non-MYCN–driven cancers, a direction for future study.

In patients with *MYCN*-amplified neuroblastoma, low immune cell infiltration including that of $CD4^+$ cells is a characteristic feature, although the underlying mechanisms are not clearly understood (*6*). Patients with high-risk disease typically have bone marrow involvement and likely reduced overall immune cell production (*62*). Studies of animal models allow us to untangle the complex events during the formation and evolution of the TME. Besides its pathological and genetic resemblance to human disease (*19*–*23*), the zebrafish model of MYCN-driven neuroblastoma provides unparalleled accessibility to the TME through live imaging. We show that Cklf-high neuroblastoma recruited $Cd4^+$ cells to tumor parenchyma as early as the premalignant stage, yet the rate of $Cd4^+$ cell infiltration decreased as tumors progressed to a much more advanced stage in older fish. Recent murine studies have provided supporting data indicating the presence of oncogenic $CD4^+$ cells in the TME (*63*). We observed the recruitment of neutrophils and macrophages to the *MYCN*-overexpressing neural crests before the arrival of $Cd4^+$ cells. These findings unveil the sequential order of immune cell recruitment and CKLF-driven interactions between innate and adaptive immune cells during the emergence of the TME.

In addition to its advantage in live imaging, the zebrafish serves as a superior model for the study of $T_{reg}$ cells. Notably, the *FOXP3* gene lies on the X chromosome in mammalian systems (*64*), making it difficult to study a true monoallelic *FOXP3* loss. In female mammals, X chromosomes are inactivated randomly in cells throughout the body, leading to both wild-type and mutant $T_{reg}$ cells (*65*). The function of wild-type $T_{reg}$ cells dominates in female *FOXP3* heterozygous mice, resulting in a phenotype indistinguishable from true wild-type animals (*65*–*67*). Zebrafish offer a unique advantage studying $T_{reg}$ cells due to the analogous *foxp3a* gene being located on a somatic chromosome (*68*).

The presence of $T_{reg}$ cells in the TME is a characteristic feature of many human tumors (*69*, *70*); however, their role is context dependent. Our studies have demonstrated the critical role of $T_{reg}$ cells in MYCN-driven cancer initiation and progression mediated through the CKLF-CCR4 interaction. Despite remarkable efforts to develop $T_{reg}$-specific therapies for multiple cancers, directly targeting $T_{reg}$ cells often triggers systemic inflammation and has not been clinically applicable (*71*, *72*). Our discovery of the crucial role of CKLF, rather than the known $T_{reg}$ chemokines CCL17 and CCL22 (*73*), in driving $T_{reg}$ cell recruitment and immunosuppression will inspire alternative therapeutic developments. Instead of directly targeting $T_{reg}$ cells, disrupting the CKLF-CCR4 interaction by antibodies or small-molecule inhibitors could uncouple the cross-talk between MYCN-activated tumors and $T_{reg}$ cells, thus relieving tumor-specific immunosuppression while sparing normal functions of $T_{reg}$ cells.

## MATERIALS AND METHODS

### CCLE analysis

Data extraction, data analysis, and figure generation for the CCLE database were performed using Python version 3.9.13. The expression of 43 chemokines was extracted from 1108 cell lines across 84 solid tumor types in the CCLE database. Each specific chemokine expression was averaged across all available cell lines for each cancer type. Cancer types were ranked on the basis of the ratio of *CKLF* expression compared to the average expression of the other chemokines. The higher the ratio, the more forward the cancer was listed to the left in Fig. 1A and fig. S1.

### Patient sample analysis

Publicly available datasets from Gene Expression Omnibus or The Cancer Genome Atlas were reanalyzed using R2: Genomics Analysis and Visualization Platform (http://r2.amc.nl), Survival Genie (https://bbisr.shinyapps.winship.emory.edu/SurvivalGenie/), cBioPortal (www.cbioportal.org), and Kaplan-Meier plotter (https://kmplot.com/analysis/) online platforms (*28*–*32*). The datasets are detailed in tables S1 to S3. The median expression value of *CKLF*, *CXCL16*, and *CXCL1* was used to categorize patients into low- and high-expression groups. Overall and event-free (for neuroblastoma patients only) survival was estimated using Kaplan-Meier scan methods and compared using the log-rank Mantel-Cox test. The R2 Kaplan scan method optimizes the survival cutoff based on statistical testing and generates a Bonferroni correction, separating the dataset into two groups based on gene expression.

### Derivation of gene signature scores and correlation analysis

Of the 157 *MYCN* signature identified by Valentijn *et al.* (*37*), 87 genes positively correlated with *MYCN* expression were ranked on the basis of their expression levels in each tumor. The percentiles were derived for each gene, and the average percentile value was calculated to determine the *MYCN* signature score (*37*). In the same way, 18 genes from Jung *et al.* (*36*) were used to calculate the *MYC* signature score. One *CKLF* gene was used to determine the *CKLF* score for each tumor.

The correlation analysis for *MYCN* signature, *MYC* signature, and *CKLF* score was performed using the R corrplot package. Pearson's correlation coefficients were calculated for all pair-wise correlations among all parameters using a correlogram. The degree of association between parameters was created and visualized using the sizes and colors of the circles.

### ChIP-seq analysis

The ChIP-seq signal (revolutions per minute per base pair) graph files were obtained through the National Center for Biotechnology Information Gene Expression Omnibus database (GSE80151) (*24*). The USCS genome browser was used to process the files to produce graphs for each cell line analyzed. An $\ln(1 + x)$ transformation of the signal was applied to graphs at the *CKLF* promoter region for all cell lines upon different treatments as described (*42*).

### Cell culture and enzyme-linked immunosorbent assay

SHEP-MYCN-ER cells were obtained from M. C. Simon's laboratory at the University of Pennsylvania (*74*), and cultured at 37°C in RPMI 1640 medium supplemented with 10% fetal bovine serum (FBS) and 5% $CO_2$. For enzyme-linked immunosorbent assay (ELISA), SHEP-MYCN-ER cells were cultured in the presence of ethanol or 500 nM 4OHT (Sigma-Aldrich, H6278) for 48 hours. The amounts of secreted CKLF (i.e., CKLF1 as it is the only secreted isoform by SHEP-MYCN-ER cells) in the medium were detected using a human CKLF ELISA kit (Novus, NBP2-75289).

### Transwell migration assay

For testing the ability of CKLF to attract $T_{reg}$ cells, medium from human SHEP-MYCN-ER cells treated with or without 4OHT for 48 hours or supplemented with synthetic C27 and C19 peptides of the secreted CKLF1 were placed in lower chambers of the transwell plates with 5-μm pore membrane (Corning). Peripheral blood mononuclear cells (PBMCs) were isolated from human

blood (Research Blood Components LLC) through centrifugation with the Ficoll Plague reagent (Cytiva) at 400*g* for 30 min, with acceleration/deceleration rates at 9/0. PBMCs were briefly incubated in RPMI 1640 medium supplemented with 10% FBS for 2 hours. To examine the effect of CCR4 blockade, PBMCs were cultured in the presence of mogamulizumab (1 μg/ml) or phosphate-buffered saline for 1 hour. Nonadherent mononuclear cells were then added to the upper chamber of the transwell plates at a density of $10^6$ cells/100 μl. The plates were incubated at 37°C supplemented with 5% $CO_2$. After 4 hours, cells from both upper and lower chambers were collected and stained with BV421-conjugated CD4 (1:100; clone RPA-TA, BioLegend, 300501), allophycocyanin (APC)/CY7-conjugated CD8 (1:100; clone SK1, BioLegend, 344702), and phycoerythrin-conjugated anti-CD25 (1:100; clone M-A251, BioLegend, 356101). These cells were subsequently fixed and permeabilized with a human FOXP3 buffer set (BD Biosciences) and then stained with Alexa Fluor 647–conjugated anti-FOXP3 monoclonal antibodies (1:100; clone 259D/C7, BD Biosciences, 560044) to identify $CD4^+CD25^+FOXP3^+$ $T_{reg}$ cells. The percentages of migrated cells were calculated by dividing the number of migrated cells in the lower chamber by the total cells of the same type.

### Immunohistochemical staining and scoring

Formalin-fixed, paraffin-embedded tumor tissue was obtained from patients with neuroblastoma that had targeted multigene sequencing at Brigham and Women's Hospital/Dana-Farber Cancer Institute (*75*). Patient samples were analyzed under Dana-Farber/Harvard Cancer Center Institutional Review Board protocol (#10-417) and Mass General Brigham Institutional Review Board approval (#2019P000017), which is a secondary use of excess human material protocol for which consent was waived. Four-micrometer-thick tissue sections were used for hematoxylin and eosin staining and immunohistochemical staining, the latter of which was performed using the Leica Bond III automated staining platform and Leica Biosystems Refine Detection Kit. The primary antibodies include anti–N-MYC (1:160 dilution; clone D4B2Y, Cell Signaling Technology, 51705; citrate antigen retrieval), anti-CKLF (1:400 dilution; clone EPR11985[2], Abcam, ab180512; EDTA antigen retrieval), and anti-FOXP3 (1:50 dilution; clone D2WE8, Cell Signaling Technology, 98377). Pancreatic tissue was used as a positive control for anti-CKLF staining and brain tissue as the negative control. The staining was analyzed by board-certified pathologists who were blinded to the samples' molecular status. Nuclear MYCN and cytoplasmic CKLF staining were assessed under ×200 magnification, using a modified *H* score (ranging from 0 to 300), in which the percentage of tumor cells with positive staining was multiplied by the staining intensity [graded from 0 (none) to 3 (strong)] as described (*76*). The score is based on tumor areas only, excluding areas with immune niches. *H* score of 50 for both MYCN and CKLF was used as the cutoff to categorize patient samples into high and low groups, respectively. The number of $FOXP3^+$ T cells was quantified at ×200 magnification, divided by the field-of-view area to obtain cell density, and then averaged across multiple fields of view.

### Zebrafish husbandry

Zebrafish husbandry and handling were performed in the aquatic facility at Boston University School of Medicine under approved protocols from the Institutional Animal Care and Use Committee. The *Tg(dβh:EGFP)* and *Tg(dβh:MYCN;dβh:EGFP)* fish in the AB wild-type background were obtained from the A. Thomas Look Laboratory at Dana-Farber Cancer Institute (*20*). The *Tg(foxp3a:EGFP)* and *foxp3a*$^{+/-}$ fish in the AB background were obtained from C. Ceol's laboratory at the University of Massachusetts Worcester (*54*). The *Tg(Cd4-1:mCherry)* fish in the AB background were obtained from A. Hurlstone's laboratory at the University of Manchester (*48*).

### Subcloning

To generate the *dβh:cklf* construct, zebrafish *cklf* cDNA was amplified using phusion high-fidelity enzyme (New England Biolabs) and cloned into the *pDONR221* gateway donor vector (Invitrogen, 12536017). The expression construct was generated by combining three entry clones—*p5E-dβh*, *pDONR221-cklf*, and *p3E-polyA*—with a modified destination vector containing I-Sce I recognition sites (*20*). The primer sequences used for subcloning include *cklf*: 5′-GGGGACAAGTTTGTACAAAAAAGCAGGCTTAATGGAAGTTGATTTGGCCTTGTTG-3′ (forward) and 5′-GGGGACCACTTTGTACAAGAAAGCTGGGTTTTACTCTTCCCCTGTTTGGGCT-3′ (reverse).

### Zebrafish genotyping and tumor surveillance

The *Tg(dβh:MYCN;dβh:EGFP)* fish were crossed with *Tg(Cd4-1:mCherry)* transgenic or *foxp3a*$^{+/-}$ mutant zebrafish to generate one–cell stage embryos, which were coinjected with *dβh:cklf* and *cmlc2:EGFP* constructs. The *Tg(dβh:MYCN;dβh:EGFP)* embryos were also coinjected with the *dβh:mCherry* construct as the controls. Cointegration of the *cmlc2:EGFP* construct (*77*), which expresses EGFP under the cardiac myosin light chain 2 promoter (*cmlc2*), served as a marker to identify the *Tg(dβh:cklf)* fish. Progenies were raised and screened at 5 days after fertilization under a fluorescent dissecting microscope (Olympus) for EGFP-expressing cell masses at the interrenal gland to confirm the presence of *MYCN* transgene. At 4 weeks of life, the sorted fish were fin-clipped to extract genomic DNA for PCR amplifications using gene-specific primers and Taq DNA polymerase (New England Biolabs). The following primers were used to identify fish harboring *foxp3a* mutations: 5′-CAGTTCTGAAGGCAAAGGG-3′ (forward) and 5′-AATCGGTGCTTATGCGTC-3′ (reverse) as previously described (*54*). Fish were monitored and imaged weekly for tumor development as described (*19*, *20*). The EGFP mass away from primary tumors were considered as sites of metastasis, which were manually counted under a fluorescent microscope after surgical dissection of fish (Olympus, MVX10). Tumor burden from the primary and metastatic tumors was quantified using ImageJ software [National Institutes of Health (NIH)].

### Frozen sectioning and confocal microscopy

Fish were euthanized as described in Institutional Animal Care and Use Committee protocols, subsequently fixed in 4% paraformaldehyde (Thermo Fisher Scientific) at 4°C overnight with gentle agitation, washed with phosphate-buffered saline containing 0.1% Tween 20 (Thermo Fisher Scientific), equilibrated in 30% sucrose at 4°C overnight, and frozen at −80°C. The frozen fish were embedded in optimal cutting temperature compound (Sakura Finetek) and sectioned at a 14-μm thickness using a cryostat (Thermo Fisher Scientific).

Live embryos and fish embedded in 1% low-melting agarose (Life Technologies) or fixed samples were imaged using LSM 710-Live Duo Confocal microscope (Zeiss). Images were processed using ImageJ software (NIH).

### Flow cytometry

Both primary and metastatic tumors were dissected under a fluorescent microscope (Olympus), dissociated in a mixture of RPMI 1640 (Corning), Liberase (0.025 μg/ml; Roche), deoxyribonuclease I (0.6 μg/ml; Thermo Fisher Scientific), and 1× penicillin/streptomycin (Corning), washed in RPMI 1640 supplemented with 10% FBS (Sigma-Aldrich), and filtered with a 40-μm filter (Falcon). Fish kidneys were dissected, dissociated, and filtered in RPMI 1640 supplemented with 10% FBS. Single-cell suspensions were stained with the primary antibodies: rat anti-fish CD4 (1:100; clone 6D1, Bio Cosmo, CAC-NIH-NA-01), CD8 (1:100; clone 2C3, Bio Cosmo, CAC-NIH-NA-02) (*78*–*80*), or anti-zebrafish Ncam1 antibody (1:100; Institute for Protein Innovation) in phosphate-buffered saline containing heparin (10 U/ml; Sigma-Aldrich), 10% FBS, and 1× penicillin/streptomycin for 30 min at 4°C. Cells were then stained with the secondary antibody, goat anti-rat APC (1:500; Invitrogen, A10540) or goat anti-human (1:200; Jackson ImmunoResearch, 109-136-170) for 30 min at 4°C and counterstained with 4′,6-diamidino-2-phenylindole (1:5000; Thermo Fisher Scientific, 62248). Analysis was performed on an LSRFortessa flow cytometer (BD Biosciences), and fluorescent-activated cell sorting (FACS) was performed on a FACSAria II (BD Biosciences). Purified cells were used for RNA extraction and qRT-PCR analysis. FlowJo software 10.4 (Tree Star) was used to analyze all flow cytometric data.

### Quantitative real-time PCR

RNA was extracted from cells using TRIzol (Thermo Fisher Scientific) and/or the RNeasy Micro Kit (QIAGEN) and subjected to genomic DNA clean-up and cDNA synthesis with QuantiTect Reverse Transcription Kit (QIAGEN). SYBR Green PCR master mix (Applied Biosystems) and a Step-One PCR instrument (Applied Biosystems) were used for the qRT-PCR reaction. The qRT-PCR primers are listed in table S5. *ACTB* or *act* expression levels were used to normalize the differences in RNA input. All reactions were performed in triplicates.

### Western blotting

Tumors were lysed in radioimmunoprecipitation assay buffer [1% NP-40, 0.1% SDS, 50 mM tris-HCl (pH 7.4), 150 mM NaCl, 0.5% sodium deoxycholate, and 1 mM EDTA] supplemented with 1× or 2× Halt protease and phosphatase inhibitor cocktail (Thermo Fisher Scientific). Primary antibodies included anti-MYCN (1:1000; Santa Cruz Biotechnology, sc-53993) and anti-actin (1:1000; Santa Cruz Biotechnology, sc-47778). Secondary antibodies included horseradish peroxidase–conjugated anti-mouse or anti-rabbit immunoglobulin G (1:2000 or 1:5000; Thermo Fisher Scientific, 31430 or 31460). Proteins were detected by enhanced chemiluminescence detection kits (Thermo Fisher Scientific), and autoradiographs were obtained with a G:BOX Chemi XT4 (Syngene) and a charge-coupled device camera. Quantification analysis was performed using Syngene GeneTools software (Syngene).

### Statistical analysis

Statistical analysis was performed with GraphPad Prism 8.0 using unpaired two-tailed *t* tests unless otherwise stated. Patient survival and zebrafish tumor onset curves were estimated using Kaplan-Meier methods and compared using the log-rank Mantel-Cox test. $*P < 0.05$, $**P < 0.01$, $***P < 0.001$, and $****P < 0.0001$.

## Supplementary Materials

**This PDF file includes:**

Supplementary Materials and Methods
Figs. S1 to S16
Tables S1 to S6
Legend for table S7
References

**Other Supplementary Material for this manuscript includes the following:**

Table S7

## REFERENCES AND NOTES


1. D. S. Rickman, J. H. Schulte, M. Eilers, The expanding world of N-MYC-driven tumors. *Cancer Discov.* **8**, 150–163 (2018).
2. R. Liu, P. Shi, Z. Wang, C. Yuan, H. Cui, Molecular mechanisms of *MYCN* dysregulation in cancers. *Front. Oncol.* **10**, 625332 (2020).
3. S. Joshi, Targeting the tumor microenvironment in neuroblastoma: Recent advances and future directions. *Cancers* **12**, 2057 (2020).
4. J. P. Layer, M. T. Kronmuller, T. Quast, D. van den Boorn-Konijnenberg, M. Effern, D. Hinze, K. Althoff, A. Schramm, F. Westermann, M. Peifer, G. Hartmann, T. Tüting, W. Kolanus, M. Fischer, J. Schulte, M. Hölzel, Amplification of N-Myc is associated with a T-cell-poor microenvironment in metastatic neuroblastoma restraining interferon pathway activity and chemokine expression. *Oncoimmunology* **6**, e1320626 (2017).
5. J. S. Wei, I. B. Kuznetsov, S. Zhang, Y. K. Song, S. Asgharzadeh, S. Sindiri, X. Wen, R. Patidar, S. Najaraj, A. Walton, J. M. G. Auvil, D. S. Gerhard, A. Yuksel, D. Catchpoole, S. M. Hewitt, P. M. Sondel, R. Seeger, J. M. Maris, J. Khan, Clinically relevant cytotoxic immune cell signatures and clonal expansion of T-cell receptors in high-risk MYCN-not-amplified human neuroblastoma. *Clin. Cancer Res.* **24**, 5673–5684 (2018).
6. P. Zhang, X. Wu, M. Basu, C. Dong, P. Zheng, Y. Liu, A. D. Sandler, MYCN amplification is associated with repressed cellular immunity in neuroblastoma: An in silico immunological analysis of TARGET database. *Front. Immunol.* **8**, 1473 (2017).
7. J. Galon, D. Bruni, Approaches to treat immune hot, altered and cold tumours with combination immunotherapies. *Nat. Rev. Drug Discov.* **18**, 197–218 (2019).
8. P. S. Hegde, D. S. Chen, Top 10 challenges in cancer immunotherapy. *Immunity* **52**, 17–35 (2020).
9. P. S. Hegde, V. Karanikas, S. Evers, The where, the when, and the how of immune monitoring for cancer immunotherapies in the era of checkpoint inhibition. *Clin. Cancer Res.* **22**, 1865–1874 (2016).
10. L. Wang, H. Geng, Y. Liu, L. Liu, Y. Chen, F. Wu, Z. Liu, S. Ling, Y. Wang, L. Zhou, Hot and cold tumors: Immunological features and the therapeutic strategies. *MedComm* **4**, e343 (2023).
11. G. M. Brodeur, R. C. Seeger, M. Schwab, H. E. Varmus, J. M. Bishop, Amplification of N-myc in untreated human neuroblastomas correlates with advanced disease stage. *Science* **224**, 1121–1124 (1984).
12. R. C. Seeger, G. M. Brodeur, H. Sather, A. Dalton, S. E. Siegel, K. Y. Wong, D. Hammond, Association of multiple copies of the N-myc oncogene with rapid progression of neuroblastomas. *N. Engl. J. Med.* **313**, 1111–1116 (1985).
13. S. B. Whittle, V. Smith, E. Doherty, S. Zhao, S. McCarty, P. E. Zage, Overview and recent advances in the treatment of neuroblastoma. *Expert Rev. Anticancer Ther.* **17**, 369–386 (2017).
14. K. J. Van Arendonk, D. H. Chung, Neuroblastoma: Tumor biology and its implications for staging and treatment. *Children* **6**, 12 (2019).
15. J. M. Maris, Recent advances in neuroblastoma. *N. Engl. J. Med.* **362**, 2202–2211 (2010).
16. J. M. Maris, M. D. Hogarty, R. Bagatell, S. L. Cohn, Neuroblastoma. *Lancet* **369**, 2106–2120 (2007).
17. N. R. Pinto, M. A. Applebaum, S. L. Volchenboum, K. K. Matthay, W. B. London, P. F. Ambros, A. Nakagawara, F. Berthold, G. Schleiermacher, J. R. Park, D. Valteau-Couanet, A. D. J. Pearson, S. L. Cohn, Advances in risk classification and treatment strategies for neuroblastoma. *J. Clin. Oncol.* **33**, 3008–3017 (2015).
18. L. Song, T. Ara, H. W. Wu, C. W. Woo, C. P. Reynolds, R. C. Seeger, Y. A. DeClerck, C. J. Thiele, R. Sposto, L. S. Metelitsa, Oncogene MYCN regulates localization of NKT cells to the site of disease in neuroblastoma. *J. Clin. Invest.* **117**, 2702–2712 (2007).
19. T. Tao, S. B. Sondalle, H. Shi, S. Zhu, A. R. Perez-Atayde, J. Peng, S. J. Baserga, A. T. Look, The pre-rRNA processing factor DEF is rate limiting for the pathogenesis of MYCN-driven neuroblastoma. *Oncogene* **36**, 3852–3867 (2017).
20. S. Zhu, J. S. Lee, F. Guo, J. Shin, A. R. Perez-Atayde, J. L. Kutok, S. J. Rodig, D. S. Neuberg, D. Helman, H. Feng, R. A. Stewart, W. Wang, R. E. George, J. P. Kanki, A. T. Look, Activated ALK collaborates with MYCN in neuroblastoma pathogenesis. *Cancer Cell* **21**, 362–373 (2012).
21. M. Kloc, R. M. Ghobrial, E. Kuchar, S. Lewicki, J. Z. Kubiak, Development of child immunity in the context of COVID-19 pandemic. *Clin. Immunol.* **217**, 108510 (2020).

22. S. Zhu, X. Zhang, N. Weichert-Leahey, Z. Dong, C. Zhang, G. Lopez, T. Tao, S. He, A. C. Wood, D. Oldridge, C. Y. Ung, J. H. van Ree, A. Khan, B. M. Salazar, E. Lummertz da Rocha, M. W. Zimmerman, F. Guo, H. Cao, X. Hou, S. J. Weroha, A. R. Perez-Atayde, D. S. Neuberg, A. Meves, M. A. McNiven, J. M. van Deursen, H. Li, J. M. Maris, A. T. Look, LMO1 synergizes with MYCN to promote neuroblastoma initiation and metastasis. *Cancer Cell* **32**, 310–323.e5 (2017).
23. N. M. Anderson, X. Qin, J. M. Finan, A. Lam, J. Athoe, R. Missiaen, N. Skuli, A. Kennedy, A. S. Saini, T. Tao, S. Zhu, I. Nissim, A. T. Look, G. Qing, M. C. Simon, H. Feng, Metabolic enzyme DLST promotes tumor aggression and reveals a vulnerability to OXPHOS inhibition in high-risk neuroblastoma. *Cancer Res.* **81**, 4417–4430 (2021).
24. K. Franciszkiewicz, A. Boissonnas, M. Boutet, C. Combadiere, F. Mami-Chouaib, Role of chemokines and chemokine receptors in shaping the effector phase of the antitumor immune response. *Cancer Res.* **72**, 6325–6332 (2012).
25. J. Barretina, G. Caponigro, N. Stransky, K. Venkatesan, A. A. Margolin, S. Kim, C. J. Wilson, J. Lehár, G. V. Kryukov, D. Sonkin, A. Reddy, M. Liu, L. Murray, M. F. Berger, J. E. Monahan, P. Morais, J. Meltzer, A. Korejwa, J. Jané-Valbuena, F. A. Mapa, J. Thibault, E. Bric-Furlong, P. Raman, A. Shipway, I. H. Engels, J. Cheng, G. K. Yu, J. Yu, P. Aspesi Jr., M. de Silva, K. Jagtap, M. D. Jones, L. Wang, C. Hatton, E. Palescandolo, S. Gupta, S. Mahan, C. Sougnez, R. C. Onofrio, T. Liefeld, L. MacConaill, W. Winckler, M. Reich, N. Li, J. P. Mesirov, S. B. Gabriel, G. Getz, K. Ardlie, V. Chan, V. E. Myer, B. L. Weber, J. Porter, M. Warmuth, P. Finan, J. L. Harris, M. Meyerson, T. R. Golub, M. P. Morrissey, W. R. Sellers, R. Schlegel, L. A. Garraway, The Cancer Cell Line Encyclopedia enables predictive modelling of anticancer drug sensitivity. *Nature* **483**, 603–607 (2012).
26. M. L. Balestrieri, A. Balestrieri, F. P. Mancini, C. Napoli, Understanding the immunoangiostatic CXC chemokine network. *Cardiovasc. Res.* **78**, 250–256 (2008).
27. K. Kohli, V. G. Pillarisetty, T. S. Kim, Key chemokines direct migration of immune cells in solid tumors. *Cancer Gene Ther.* **29**, 10–21 (2022).
28. B. Dwivedi, H. Mumme, S. Satpathy, S. S. Bhasin, M. Bhasin, Survival Genie, a web platform for survival analysis across pediatric and adult cancers. *Sci. Rep.* **12**, 3069 (2022).
29. E. Cerami, J. Gao, U. Dogrusoz, B. E. Gross, S. O. Sumer, B. A. Aksoy, A. Jacobsen, C. J. Byrne, M. L. Heuer, E. Larsson, Y. Antipin, B. Reva, A. P. Goldberg, C. Sander, N. Schultz, The cBio cancer genomics portal: An open platform for exploring multidimensional cancer genomics data. *Cancer Discov.* **2**, 401–404 (2012).
30. J. Gao, B. A. Aksoy, U. Dogrusoz, G. Dresdner, B. Gross, S. O. Sumer, Y. Sun, A. Jacobsen, R. Sinha, E. Larsson, E. Cerami, C. Sander, N. Schultz, Integrative analysis of complex cancer genomics and clinical profiles using the cBioPortal. *Sci. Signal.* **6**, pl1 (2013).
31. B. Gyorffy, Discovery and ranking of the most robust prognostic biomarkers in serous ovarian cancer. *Geroscience* **45**, 1889–1898 (2023).
32. B. Gyorffy, Survival analysis across the entire transcriptome identifies biomarkers with the highest prognostic power in breast cancer. *Comput. Struct. Biotechnol. J.* **19**, 4101–4109 (2021).
33. Z. X. Yue, C. Huang, C. Gao, T. Y. Xing, S. G. Liu, X. J. Li, Q. Zhao, X. S. Wang, W. Zhao, M. Jin, X. L. Ma, MYCN amplification predicts poor prognosis based on interphase fluorescence in situ hybridization analysis of bone marrow cells in bone marrow metastases of neuroblastoma. *Cancer Cell Int.* **17**, 43 (2017).
34. A. Albihn, J. I. Johnsen, M. A. Henriksson, MYC in oncogenesis and as a target for cancer therapies. *Adv. Cancer Res.* **107**, 163–224 (2010).
35. W. Zhang, Y. Yu, F. Hertwig, J. Thierry-Mieg, W. Zhang, D. Thierry-Mieg, J. Wang, C. Furlanello, V. Devanarayan, J. Cheng, Y. Deng, B. Hero, H. Hong, M. Jia, L. Li, S. M. Lin, Y. Nikolsky, A. Oberthuer, T. Qing, Z. Su, R. Volland, C. Wang, M. D. Wang, J. Ai, D. Albanese, S. Asgharzadeh, S. Avigad, W. Bao, M. Bessarabova, M. H. Brilliant, B. Brors, M. Chierici, T. M. Chu, J. Zhang, R. G. Grundy, M. M. He, S. Hebbring, H. L. Kaufman, S. Lababidi, L. J. Lancashire, Y. Li, X. X. Lu, H. Luo, X. Ma, B. Ning, R. Noguera, M. Peifer, J. H. Phan, F. Roels, C. Rosswog, S. Shao, J. Shen, J. Theissen, G. P. Tonini, J. Vandesompele, P. Y. Wu, W. Xiao, J. Xu, W. Xu, J. Xuan, Y. Yang, Z. Ye, Z. Dong, K. K. Zhang, Y. Yin, C. Zhao, Y. Zheng, R. D. Wolfinger, T. Shi, L. H. Malkas, F. Berthold, J. Wang, W. Tong, L. Shi, Z. Peng, M. Fischer, Comparison of RNA-seq and microarray-based models for clinical endpoint prediction. *Genome Biol.* **16**, 133 (2015).
36. M. Jung, A. J. Russell, B. Liu, J. George, P. Y. Liu, T. Liu, A. DeFazio, D. D. L. Bowtell, A. Oberthuer, W. B. London, J. I. Fletcher, M. Haber, M. D. Norris, M. J. Henderson, A Myc activity signature predicts poor clinical outcomes in Myc-associated cancers. *Cancer Res.* **77**, 971–981 (2017).
37. L. J. Valentijn, J. Koster, F. Haneveld, R. A. Aissa, P. van Sluis, M. E. C. Broekmans, J. J. Molenaar, J. van Nes, R. Versteeg, Functional MYCN signature predicts outcome of neuroblastoma irrespective of MYCN amplification. *Proc. Natl. Acad. Sci. U.S.A.* **109**, 19190–19195 (2012).
38. T. Berry, W. Luther, N. Bhatnagar, Y. Jamin, E. Poon, T. Sanda, D. Pei, B. Sharma, W. R. Vetharoy, A. Hallsworth, Z. Ahmad, K. Barker, L. Moreau, H. Webber, W. Wang, Q. Liu, A. Perez-Atayde, S. Rodig, N.-K. Cheung, F. Raynaud, B. Hallberg, S. P. Robinson, N. S. Gray, A. D. J. Pearson, S. A. Eccles, L. Chesler, R. E. George, The ALK(F1174L) mutation potentiates the oncogenic activity of MYCN in neuroblastoma. *Cancer Cell* **22**, 117–130 (2012).
39. M. W. Zimmerman, Y. Liu, S. He, A. D. Durbin, B. J. Abraham, J. Easton, Y. Shao, B. Xu, S. Zhu, X. Zhang, Z. Li, N. Weichert-Leahey, R. A. Young, J. Zhang, A. T. Look, MYC drives a subset of high-risk pediatric neuroblastomas and is activated through mechanisms including enhancer hijacking and focal enhancer amplification. *Cancer Discov.* **8**, 320–335 (2018).
40. J. A. Seier, J. Reinhardt, K. Saraf, S. S. Ng, J. P. Layer, D. Corvino, K. Althoff, F. A. Giordano, A. Schramm, M. Fischer, M. Holzel, Druggable epigenetic suppression of interferon-induced chemokine expression linked to MYCN amplification in neuroblastoma. *J. Immunother. Cancer* **9**, e001335 (2021).
41. W. Lutz, M. Stohr, J. Schurmann, A. Wenzel, A. Lohr, M. Schwab, Conditional expression of N-myc in human neuroblastoma cells increases expression of alpha-prothymosin and ornithine decarboxylase and accelerates progression into S-phase early after mitogenic stimulation of quiescent cells. *Oncogene* **13**, 803–812 (1996).
42. R. Zeid, M. A. Lawlor, E. Poon, J. M. Reyes, M. Fulciniti, M. A. Lopez, T. G. Scott, B. Nabet, M. A. Erb, G. E. Winter, Z. Jacobson, D. R. Polaski, K. L. Karlin, R. A. Hirsch, N. P. Munshi, T. F. Westbrook, L. Chesler, C. Y. Lin, J. E. Bradner, Enhancer invasion shapes MYCN-dependent transcriptional amplification in neuroblastoma. *Nat. Genet.* **50**, 515–523 (2018).
43. J. H. Schulte, S. Horn, T. Otto, B. Samans, L. C. Heukamp, U. C. Eilers, M. Krause, K. Astrahantseff, L. Klein-Hitpass, R. Buettner, A. Schramm, H. Christiansen, M. Eilers, A. Eggert, B. Berwanger, MYCN regulates oncogenic MicroRNAs in neuroblastoma. *Int. J. Cancer* **122**, 699–704 (2008).
44. Y. Wang, Y. Zhang, W. Han, D. Li, L. Tian, C. Yin, D. Ma, Two C-terminal peptides of human CKLF1 interact with the chemokine receptor CCR4. *Int. J. Biochem. Cell Biol.* **40**, 909–919 (2008).
45. L. A. Marshall, S. Marubayashi, A. Jorapur, S. Jacobson, M. Zibinsky, O. Robles, D. X. Hu, J. J. Jackson, D. Pookot, J. Sanchez, M. Brovarney, A. Wadsworth, D. Chian, D. Wustrow, P. D. Kassner, G. Cutler, B. Wong, D. G. Brockstedt, O. Talay, Tumors establish resistance to immunotherapy by regulating $T_{reg}$ recruitment via CCR4. *J. Immunother. Cancer* **8**, e000764 (2020).
46. H. H. Chang, Y. F. Tseng, M. Y. Lu, Y. L. Yang, S. W. Chou, D. T. Lin, K. H. Lin, S. T. Jou, W. M. Hsu, Y. M. Jeng, MYCN RNA levels determined by quantitative in situ hybridization is better than MYCN gene dosages in predicting the prognosis of neuroblastoma patients. *Mod. Pathol.* **33**, 531–540 (2020).
47. F. Westermann, D. Muth, A. Benner, T. Bauer, K. O. Henrich, A. Oberthuer, B. Brors, T. Beissbarth, J. Vandesompele, F. Pattyn, B. Hero, R. Konig, M. Fischer, M. Schwab, Distinct transcriptional MYCN/c-MYC activities are associated with spontaneous regression or malignant progression in neuroblastomas. *Genome Biol.* **9**, R150 (2008).
48. C. T. Dee, R. T. Nagaraju, E. I. Athanasiadis, C. Gray, L. Fernandez Del Ama, S. A. Johnston, C. J. Secombes, A. Cvejic, A. F. L. Hurlstone, CD4-transgenic zebrafish reveal tissue-resident Th2- and regulatory t cell-like populations and diverse mononuclear phagocytes. *J. Immunol.* **197**, 3520–3530 (2016).
49. D. Soroldoni, B. M. Hogan, A. C. Oates, Simple and efficient transgenesis with meganuclease constructs in zebrafish. *Methods Mol. Biol.* **546**, 117–130 (2009).
50. K. Z. Miao, G. Y. Kim, G. K. Meara, X. Qin, H. Feng, Tipping the scales with zebrafish to understand adaptive tumor immunity. *Front. Cell Dev. Biol.* **9**, 660969 (2021).
51. F. Ellett, L. Pase, J. W. Hayman, A. Andrianopoulos, G. J. Lieschke, Mpeg1 promoter transgenes direct macrophage-lineage expression in zebrafish. *Blood* **117**, e49–e56 (2011).
52. C. Hall, M. V. Flores, T. Storm, K. Crosier, P. Crosier, The zebrafish lysozyme C promoter drives myeloid-specific expression in transgenic fish. *BMC Dev. Biol.* **7**, 42 (2007).
53. J. B. Wing, A. Tanaka, S. Sakaguchi, Human $FOXP3^+$ regulatory t cell heterogeneity and function in autoimmunity and cancer. *Immunity* **50**, 302–316 (2019).
54. M. Kasheta, C. A. Painter, F. E. Moore, R. Lobbardi, A. Bryll, E. Freiman, D. Stachura, A. B. Rogers, Y. Houvras, D. M. Langenau, C. J. Ceol, Identification and characterization of T reg-like cells in zebrafish. *J. Exp. Med.* **214**, 3519–3530 (2017).
55. F. Ghiringhelli, P. E. Puig, S. Roux, A. Parcellier, E. Schmitt, E. Solary, G. Kroemer, F. Martin, B. Chauffert, L. Zitvogel, Tumor cells convert immature myeloid dendritic cells into TGF-beta-secreting cells inducing CD4+CD25+ regulatory T cell proliferation. *J. Exp. Med.* **202**, 919–929 (2005).
56. B. Hoechst, L. A. Ormandy, M. Ballmaier, F. Lehner, C. Kruger, M. P. Manns, T. F. Greten, F. Korangy, A new population of myeloid-derived suppressor cells in hepatocellular carcinoma patients induces CD4(+)CD25(+)Foxp3(+) T cells. *Gastroenterology* **135**, 234–243 (2008).
57. F. Ihara, D. Sakurai, M. Takami, T. Kamata, N. Kunii, K. Yamasaki, T. Iinuma, T. Nakayama, S. Motohashi, Y. Okamoto, Regulatory T cells induce $CD4^-$ NKT cell anergy and suppress NKT cell cytotoxic function. *Cancer Immunol. Immunother.* **68**, 1935–1947 (2019).
58. J. E. Jang, C. H. Hajdu, C. Liot, G. Miller, M. L. Dustin, D. Bar-Sagi, Crosstalk between regulatory T cells and tumor-associated dendritic cells negates anti-tumor immunity in pancreatic cancer. *Cell Rep.* **20**, 558–571 (2017).
59. M. V. Ruiz-Perez, A. B. Henley, M. Arsenian-Henriksson, The MYCN protein in health and disease. *Genes (Basel)* **8**, 113 (2017).
60. J. Dzieran, A. Rodriguez Garcia, U. K. Westermark, A. B. Henley, E. Eyre Sanchez, C. Trager, H. J. Johansson, J. Lehtio, M. Arsenian-Henriksson, MYCN-amplified neuroblastoma

maintains an aggressive and undifferentiated phenotype by deregulation of estrogen and NGF signaling. *Proc. Natl. Acad. Sci. U.S.A.* **115**, E1229–E1238 (2018).
61. W. M. Grady, M. Yu, S. D. Markowitz, Epigenetic alterations in the gastrointestinal tract: Current and emerging use for biomarkers of cancer. *Gastroenterology* **160**, 690–709 (2021).
62. F. Morandi, M. V. Corrias, V. Pistoia, Evaluation of bone marrow as a metastatic site of human neuroblastoma. *Ann. N. Y. Acad. Sci.* **1335**, 23–31 (2015).
63. L. A. Van de Velde, E. K. Allen, J. C. Crawford, T. L. Wilson, C. S. Guy, M. Russier, L. Zeitler, A. Bahrami, D. Finkelstein, S. Pelletier, S. Schultz-Cherry, P. G. Thomas, P. J. Murray, Neuroblastoma formation requires unconventional CD4 T cells and arginase-1-dependent myeloid cells. *Cancer Res.* **81**, 5047–5059 (2021).
64. P. Mertowska, S. Mertowski, M. Podgajna, E. Grywalska, The importance of the transcription factor Foxp3 in the development of primary immunodeficiencies. *J. Clin. Med.* **11**, 947 (2022).
65. M. A. Gavin, T. R. Torgerson, E. Houston, P. DeRoos, W. Y. Ho, A. Stray-Pedersen, E. L. Ocheltree, P. D. Greenberg, H. D. Ochs, A. Y. Rudensky, Single-cell analysis of normal and FOXP3-mutant human T cells: FOXP3 expression without regulatory T cell development. *Proc. Natl. Acad. Sci. U.S.A.* **103**, 6659–6664 (2006).
66. D. Zemmour, L. M. Charbonnier, J. Leon, E. Six, S. Keles, M. Delville, M. Benamar, S. Baris, J. Zuber, K. Chen, B. Neven, M. I. Garcia-Lloret, F. M. Ruemmele, C. Brugnara, N. Cerf-Bensussan, F. Rieux-Laucat, M. Cavazzana, I. Andre, T. A. Chatila, D. Mathis, C. Benoist, Single-cell analysis of FOXP3 deficiencies in humans and mice unmasks intrinsic and extrinsic $CD4^+$ T cell perturbations. *Nat. Immunol.* **22**, 607–619 (2021).
67. J. van der Veeken, C. Campbell, Y. Pritykin, M. Schizas, J. Verter, W. Hu, Z. M. Wang, F. Matheis, D. Mucida, L. M. Charbonnier, T. A. Chatila, A. Y. Rudensky, Genetic tracing reveals transcription factor Foxp3-dependent and Foxp3-independent functionality of peripherally induced Treg cells. *Immunity* **55**, 1173–1184.e7 (2022).
68. X. Li, F. Zhang, N. Wu, D. Ye, Y. Wang, X. Zhang, Y. Sun, Y. A. Zhang, A critical role of foxp3a-positive regulatory T cells in maintaining immune homeostasis in zebrafish testis development. *J. Genet. Genomics* **47**, 547–561 (2020).
69. A. Facciabene, G. T. Motz, G. Coukos, T-regulatory cells: Key players in tumor immune escape and angiogenesis. *Cancer Res.* **72**, 2162–2171 (2012).
70. G. Oliveira, K. Stromhaug, N. Cieri, J. B. Iorgulescu, S. Klaeger, J. O. Wolff, S. Rachimi, V. Chea, K. Krause, S. S. Freeman, W. Zhang, S. Li, D. A. Braun, D. Neuberg, S. A. Carr, K. J. Livak, D. T. Frederick, E. F. Fritsch, M. Wind-Rotolo, N. Hacohen, M. Sade-Feldman, C. H. Yoon, D. B. Keskin, P. A. Ott, S. J. Rodig, G. M. Boland, C. J. Wu, Landscape of helper and regulatory antitumour $CD4^+$ T cells in melanoma. *Nature* **605**, 532–538 (2022).
71. H. Van Damme, B. Dombrecht, M. Kiss, H. Roose, E. Allen, E. Van Overmeire, D. Kancheva, L. Martens, A. Murgaski, P. M. R. Bardet, G. Blancke, M. Jans, E. Bolli, M. S. Martins, Y. Elkrim, J. Dooley, L. Boon, J. K. Schwarze, F. Tacke, K. Movahedi, N. Vandamme, B. Neyns, S. Ocak, I. Scheyltjens, L. Vereecke, F. A. Nana, P. Merchiers, D. Laoui, J. A. Van Ginderachter, Therapeutic depletion of $CCR8^+$ tumor-infiltrating regulatory T cells elicits antitumor immunity and synergizes with anti-PD-1 therapy. *J. Immunother. Cancer* **9**, e001749 (2021).
72. A. Tanaka, S. Sakaguchi, Targeting Treg cells in cancer immunotherapy. *Eur. J. Immunol.* **49**, 1140–1146 (2019).
73. O. Yoshie, CCR4 as a therapeutic target for cancer immunotherapy. *Cancers* **13**, 5542 (2021).
74. G. Qing, B. Li, A. Vu, N. Skuli, Z. E. Walton, X. Liu, P. A. Mayes, D. R. Wise, C. B. Thompson, J. M. Maris, M. D. Hogarty, M. C. Simon, ATF4 regulates MYC-mediated neuroblastoma cell death upon glutamine deprivation. *Cancer Cell* **22**, 631–644 (2012).
75. E. P. Garcia, A. Minkovsky, Y. Jia, M. D. Ducar, P. Shivdasani, X. Gong, A. H. Ligon, L. M. Sholl, F. C. Kuo, L. E. MacConaill, N. I. Lindeman, F. Dong, Validation of OncoPanel: A targeted next-generation sequencing assay for the detection of somatic variants in cancer. *Arch. Pathol. Lab. Med.* **141**, 751–758 (2017).
76. E. Specht, D. Kaemmerer, J. Sanger, R. M. Wirtz, S. Schulz, A. Lupp, Comparison of immunoreactive score, HER2/neu score and H score for the immunohistochemical evaluation of somatostatin receptors in bronchopulmonary neuroendocrine neoplasms. *Histopathology* **67**, 368–377 (2015).
77. M. Rembold, K. Lahiri, N. S. Foulkes, J. Wittbrodt, Transgenesis in fish: Efficient selection of transgenic fish by co-injection with a fluorescent reporter construct. *Nat. Protoc.* **1**, 1133–1139 (2006).
78. H. Toda, Y. Saito, T. Koike, F. Takizawa, K. Araki, T. Yabu, T. Somamoto, H. Suetake, Y. Suzuki, M. Ototake, T. Moritomo, T. Nakanishi, Conservation of characteristics and functions of CD4 positive lymphocytes in a teleost fish. *Dev. Comp. Immunol.* **35**, 650–660 (2011).
79. H. Toda, Y. Shibasaki, T. Koike, M. Ohtani, F. Takizawa, M. Ototake, T. Moritomo, T. Nakanishi, Alloantigen-specific killing is mediated by CD8-positive T cells in fish. *Dev. Comp. Immunol.* **33**, 646–652 (2009).
80. Y. Shibasaki, Y. Matsuura, H. Toda, N. Imabayashi, T. Nishino, K. Uzumaki, C. Hatanaka, T. Yabu, T. Moritomo, T. Nakanishi, Kinetics of lymphocyte subpopulations in allogeneic grafted scales of ginbuna crucian carp. *Dev. Comp. Immunol.* **52**, 75–80 (2015).
81. Z. Su, H. Fang, H. Hong, L. Shi, W. Zhang, W. Zhang, Y. Zhang, Z. Dong, L. J. Lancashire, M. Bessarabova, X. Yang, B. Ning, B. Gong, J. Meehan, J. Xu, W. Ge, R. Perkins, M. Fischer, W. Tong, An investigation of biomarkers derived from legacy microarray data for their utility in the RNA-seq era. *Genome Biol.* **15**, 523 (2014).
82. H. Kocak, S. Ackermann, B. Hero, Y. Kahlert, A. Oberthuer, D. Juraeva, F. Roels, J. Theissen, F. Westermann, H. Deubzer, V. Ehemann, B. Brors, M. Odenthal, F. Berthold, M. Fischer, Hox-C9 activates the intrinsic pathway of apoptosis and is associated with spontaneous regression in neuroblastoma. *Cell Death Dis.* **4**, e586 (2013).

**Acknowledgments:** We thank C. Yan, D. M. Langenau, A. Hurlstone, N. M. Anderson, and M. C. Simon for reagents; K. Miao for technical assistance; Y. Zhou and L. Zon for discussions; S. Cui for equipment; M. T. Kirber from the Imaging Core Facility at Boston University School of Medicine for expert help with imaging acquisitions; R. Mathieu from Boston Children's Hospital Flow Cytometry Core Facility for assistance with cell sorting; and C. Edwards and the Dana-Farber/Harvard Cancer Center Specialized Histopathology Core for immunohistochemistry services. **Funding:** This study was supported by grants from the NIH (CA134743 and CA215059), the St. Baldrick's Foundation, the National Science Foundation (1911253), the American Cancer Society (RSG-17-204-01-TBG), and the Alex's Lemonade Stand Foundation to H.F. X.Q. is supported by a Warren Alpert Distinguished Scholars Fellowship. X.Z. is supported by a postdoctoral fellowship from the China Scholarship Council (no. 201808440648). S.S. is supported by a Young Investigator Award from the Rally Foundation for Childhood Cancer Research and the Friends for Life Neuroblastoma Fellowship. J.B.I. acknowledges support from the NIH (K12CA090354) and Conquer Cancer Foundation. A.E.F. and K.S.S. are supported by the Undergraduate Research Opportunity Program from Boston University. H.N. received the support through a POST award from the Alex's Lemonade Stand Foundation. D.B.K. is supported by a grant from the NIH (R01HL157174). R.E.G. acknowledges support from the St. Baldrick's Foundation, a DoD Idea Award (CA191000), and an NIH grant (R01CA271605). The Dana-Farber/Harvard Cancer Center is supported in part by an NCI Cancer Center Support Grant (NIH P30CA06516). The content of this research is solely the responsibility of the authors and does not necessarily represent the official views of the NIH. **Author contributions:** H.F. and X.Q. conceived the project. H.F., X.Q., A.L., X.Z., S.S., and R.E.G. designed the experiments. X.Q., A.L., X.Z., H.N., M.R., C.K., G.K.M., A.E.F., K.S.S., D.K., S.S., and L.K. performed the experiments. X.Q., X.Z., A.L., H.N., M.R., S.D., A.E.F., S.S., D.V., L.K., T.Z., and H.F. analyzed the data. J.B.I., T.Z., and S.A. designed, implemented, and analyzed the immunohistochemistry experiments. K.L., R.M., C.C., D.B.K., C.J.W., and R.T.N. provided reagents and advice. X.Q., H.F., X.Z., G.K.M., A.E.F., L.K., D.K., and R.E.G. wrote the manuscript with inputs from all other authors. H.F. and R.E.G. supervised the project. R.E.G., S.S., C.C., D.B.K., J.B.I., L.L., C.-T.L., C.J.W., and R.T.N. provided experimental support and intellectual inputs. **Competing interests:** D.B.K. is a scientific advisor for Immunitrack, a wholly owned subsidiary of Eli Lilly and Company and Breakbio. D.B.K. owns equity in Affimed N.V., Agenus Bio., Armata Pharmaceuticals, Breakbio, BioMarin Pharmaceutical, Celldex Therapeutics, Editas Medicine, Gilead Sciences, Immunitybio, and Lexicon Pharmaceuticals. BeiGene, a Chinese biotech company, supported unrelated severe acute respiratory syndrome coronavirus 2 research at TIGL. C.J.W. holds equity in BioNTech and receives research funding from Pharmacyclics, and is on the advisory boards of Repertoire and Aethon. X.Q. and H.F. filed a provisional patent sponsored by the Trustees of Boston University. The authors declare that they have no other competing interests. **Data and materials availability:** All data needed to evaluate the conclusions in the paper are present in the paper and/or the Supplementary Materials. The constructs generated in this research will be available for distribution after completing a material transfer agreement with Boston University. All raw data for this research are included as an excel file: table S7. All Python code used in this study is publicly archived on Zenodo (https://doi.org/10.5281/zenodo.10199258). The zebrafish Ncam-1 antibody—IPI-zNcam-1—used as a marker for NK cells is available for research studies from The Institute for Protein Innovation. For more information, contact antibodies@proteininnovation.org.

Submitted 24 March 2023
Accepted 8 February 2024
Published 15 March 2024
10.1126/sciadv.adh9547